Quantum Gas Microscope With Optical Lattice

A dissertation presented

by

Amy Wan-Chih Peng

to

The Department of Physics

in partial fulfillment of the requirements

for the degree of

Doctor of Philosophy

in the subject of

Physics

Harvard University

Cambridge, Massachusetts

May 2010

Thesis advisor   Author

Markus Greiner   **Amy Wan-Chih Peng**

Quantum Gas Microscope With Optical Lattice

Abstract

In this thesis, we demonstrate the feasibility of single site resolution in a two dimensional optical lattice with submicron lattice spacing, suitable for studying condensed matter Hamiltonians in the strong interacting regime. With the combination of magnetic and optical manipulation of atoms, we show how to reproducibly generate two dimensional Bose Einstein Condensates of ^{87}Rb situated at the focus of our "Quantum Gas Microscope", allowing us to utilise the high numerical aperture for both lattice generation and single atom detection. We then give preliminary evidence of superfluid to mott insulator transition in this setup.

Contents

Acknowledgments

It was often said, that the graduate school experience will change one's life, for better or worse. Without doubt, the last five years were for me, an incredible path full of trials and tribulations from which I had emerged with immense intellectual and personal growth. I can honestly claim that I will leave here a wiser person from whence I came. Foremostly, I owe a deep gratitude to my family for giving me the courage and upbringing to be here in the first place.

The success of the experiment would not have been possible without the astute leadership and tireless hardwork of the four people that led the experiment during my time here : Markus Greiner, Jonathon Gillen, Waseem Bakr and Simon Foelling. Without their ingenuity and tenacity, I would be unable to write these words today. To them, I express my indebtedness for their guidance and the generosity they had shown me.

Much of my years had been made more fun by the members of the "Center for Cool Technology". To Widagdo Setiawan, Florian Huber, Kate Wooley-Brown and Toby Schuster, for teaching me about computers, electronics and the unhealthy diet of lab snacks. I also thank the past members of Greiner lab whose invaluable work made it possible to do my, Edward Su, Peter Unterwidter, Hannes Brachmann, and my best wishes for the future of the experiment, Eric Tai and Alex Ma.

Many amazing people had contributed to making my life more colourful at Harvard. Amongst them, Daniyar Nurgliev, Alexey Gorshkov, Jonathan Ruel, Brandan Shields, Susanne Pielawa, Anne Sung, Andy Sisson, Stephanie Bush, Susan Choi, Allysa Adams, Christina Smiraglia, Yu-Ju Lin, David Simpson, Jane Lee, Christian Weedbrook, Jason Lo and Magnus Hsu. I thank them all for sharing this exhilarating journey with me.

Finally, there are three people who had stood beside me, without whom I would have given up a long time ago. Haruka Tanji, with her infinite wisdom and foresight that so frequently saved me from self destruction; Yulia Gurevich, for always listening patiently

and never once had any doubt in me; and the one whose strength I leaned on in times good

and bad, Jarek Labaziewicz for holding my hands when I needed him the most.

I dedicate the work giving rise to this thesis, to these three remarkable individuals : to Haruka, for inspiring me to be tall and strong; to Yulia who showed me the true meaning of grace; and to Jarek, who taught me how to live.

Chapter 1

Introduction

1.1 Optical Lattice As A Tool For Condensed Matter

The achievement of Bose Einstein Condensation [36, 37, 38] (BEC) and degenerate Fermi gas [39, 40, 41] using ultra-cold dilute gases has ushered in a new era of exciting research in recent years. Not only has it expanded the frontier of our understanding in atomic and molecular physics, but also merged these fields with that of condensed matter physics, where ultra-cold atomic experiments could achieve what was previously thought impossible with real solids.

The initial experiments on these weakly interacting gases focussed mainly on phenomenons related to the existence of a macroscopic wavefunction for the many body system. It was realised earlier on, that just like superfluidity, Bose Einstein condensates could be described by a single macroscopic wavefunction (also known as order parameter) which describes *all* the particles within the condensate. However, unlike the original motivator of superfluidity, ^{4}He, for which this description is only phenomenological due to the strong interactions which creates uncondensed atoms from condensed ones, dilute gas BEC on the other hand, are so weakly interacting to be essentially pure condensates at sufficiently low

temperatures. The behaviour of the ensemble is adequately described by the time evolution of the macroscopic/condensate wavefunction where interaction appears only as an additional potential dependent on the local density of atoms [51]. Therefore, in dilute gases the zeroth order solution to the many body problem reduces effectively to a single particle problem. Small fluctuations around this mean value are well described by the Bogoliubov theory which decomposes excitations into non-interacting quasi-particle modes. The validity of these description for dilute gases has been verified quantitatively by several experiments.

To reach into the realm of condensed matter physics, one needs to make the dilute gas strongly interacting such that a description in terms of independent quasi-particles is no longer adequate. Two methods have emerged so far for accomplishing this task, (i) the use of Feshbach resonance to change the scattering length of the atoms and (ii) placing the condensate into a periodic potential created by light, also known as an optical lattice. For bosons, the use of Feshbach resonance creates extraneous losses in condensate fraction due to three body loss [61, 62], so it's not a feasible route towards strong interaction. In this thesis, we describe our path for reaching correlated many-body systems using ^{87}Rb condensates in an optical lattice.

Atoms in optical lattices achieves strong interaction by changing the relative magnitudes of the interaction energy and the kinetic energy. At low lattice depth, the atoms favour delocalisation over the entire lattice, since the resultant reduction in kinetic energy is more than sufficient to compensate for the increase in interaction energy incurred from having multiple atoms per lattice site [1]. The situation is reversed as the lattice depth is increased. Tunneling becomes prohibitively expensive in comparison to the energy cost of having multiple atoms per lattice site. The dominant energy scale is then set by the

---

[1]Unlike electrons, interaction between neutral atoms is very short ranged, so that two atoms only interact when they happen to occupy the same lattice site

interaction energy, thus reaching the regime of strongly interacting.

It was not long, before the community started to recognise the advantages of the optical lattice system over the traditional model system for studying condensed matter - that of real solids. In essence, atoms tunneling in the optical lattice is entirely analogous to electrons tunneling within the periodic potential due to the nuclei of a crystalline material [63]. Indeed, many of the theoretical models that were first motivated by real solids, such as the Hubbard model for describing transition from conducting to insulating phases in metals, have now found parallel realisations using atoms in optical lattice [26].

But there are several advantages to the neutral atoms in lattice toolbox not possible with real solids. First, the energy scales of the optical lattice system is much lower (in the Hz range) than in real solids (in the thousands of THz range), which means that dynamics occurs on a slow enough time scale to allow observation in real time. With the advent of high spatial resolution, such as that described in this thesis, one could observe single atom time evolution within the lattice, analogous to observing a single electron's dynamic in a solid. Secondly, the optical lattice system affords a much cleaner and controllable system than real solids where defect free and arbitrary lattice potentials could be created and manipulated dynamically. Coupled with single site addressability, known initial states could be prepared either by direct manipulation of the atoms in the lattice or by projective measurements [68].

A spectacular demonstration of some of the above features was the observation of Bloch oscillations using cold cesium atoms in a one dimensional optical lattice [23]. Although it was first theoretical predicted in 1929 [66, 67], Bloch oscillations were not observable in natural crystals until 1993, due to the presence of lattice defects [65] [2]. The

---

[2]Electron scattering time off lattice defects were much shorter than the Bloch oscillation period, preventing their observation until the invention of semiconductor superlattices whose large lattice spacing allows for much shorter Bloch periods so that Bloch oscillations to be observed from THz emission of electrons

optical lattice system is thus an implementation of a "quantum simulator" that was first purposed by Richard Feynman [49, 50] where one may realise model Hamiltonians from condensed matter theory in a much cleaner and controlled way.

1.2   Single Site Resolution

In this thesis, we concentrate on combining the recent achievement of optical single site resolution [48] with the use of optical lattice potential to study the behaviours of strongly correlated many body systems. Even though the current state of technology for generating and controlling atoms in optical lattices is rather advanced, most detection methods to date, still relies on absorption imaging typically applied after time of flight in order to reduce the optical density of the cloud to below saturation [3]. Although in-situ detection techniques such as phase contrast imaging exists, there is usually insufficient spatial resolution to detect features on the scale of a few lattice sites which is particularly pertinent for experiments involving inhomogeneous systems where multiple phases of matter coexists in the ensemble but are separated spatially. Catering to the growing need for a versatile, high resolution imaging method, several groups have recently approached the problem with different techniques. One method, with the highest spatial resolution to date (about 150 nm) was achieved using the same principles as a scanning electron microscope [69].

In this experiment, we accomplish high resolution in-situ detection via fluorescence imaging using a high numerical aperture microscope for the atoms in the lattice, similar to that demonstrate in [70] for a 5μm lattice spacing. Our imaging system, or quantum gas microscope utilises the concept of solid immersion microscopy [20] : by placing the atoms

---

[3]Absorption imaging of in-situ cesium atoms in a two dimensional optical lattice was recently carried out with 3 μm spatial resolution in [15]

very close to a glass surface with refractive index greater than 1, we can increase the numerical aperture without having to increase the physical size of our lenses to impossible values. We then integrate the optical lattice with the microscope system by using it as a part of the imaging system which projects the optical lattice pattern imprinted on a transmission phase hologram, onto the location of the atoms. The high numerical aperture of the microscope allows us to image the lattice with great demagnification, creating optical lattices with small lattice spacing that is a pre-requisite for studying many body physics in optical lattices. At the same time, the lattice projection method allows us to conveniently produce patterned potentials for the atoms simply by changing the graphics on the transmission hologram. With the advent of computer controlled holograms such as a spatial light modulator, it is even possible to produce dynamically varying lattice potentials.

This thesis describes in details, the setup of the second generation of the quantum gas microscope which allows us to perform experiments with more reproducibility than the first generation of the apparatus. With a simple cubic lattice, we study the Bose Hubbard hamiltonian [13] with our optical lattice system, and present the first evidence of the superfluid to mott insulator transition in our experiment directly observed in-situ using the quantum gas microscope.

1.3 Overview

- The second chapter review theory of weakly interacting Bose gas and the phenomenon of Bose Einstein condensation as well as interaction of atoms with light fields which gives us the ability to create optical lattice potentials.

- The third chapter describes the details of the quantum gas microscope and the pro-

cedures that we use to detect atoms on a single lattice site.

- In the fourth chapter, the details of the two dimensional optical trap for the atoms is presented. This part of the experiment generated atomic ensemble in a suitable configuration for use with the high resolution imaging and projection of the optical lattice potential.

- The fifth chapter presents theoretical treatment of atoms in optical lattice and the Bose Hubbard hamiltonian which we simulate with our apparatus.

- The sixth chapter presents experimental evidence of the superfluid to mott insulator transition in our lattice.

Chapter 2

Basic Condensate Physics

This chapter briefly summarise the theoretical concepts of Bose Einstein Condensation (BEC), in particular, the case of a two dimensional BEC in a harmonic trap that is of relevance to our experiment. We also outline the principles behind the optical dipole force which is the main mechanism by which we manipulate the atoms.

2.1 Condensation Phenomenon

The concept of Bose Einstein Condensation (BEC) was first purposed by Bose and Einstein in 1924 [9]. One can think of BEC as occurring when the thermal de Broglie wavelength characterizing the extent of each atom's wavepacket

$$\lambda_{dB} = \sqrt{\frac{h^2}{2\pi m k_B T}} \tag{2.1}$$

becomes on order of the interatomic distance. Equation (2.1) clearly indicates that this occurs at very low temperatures. When this occurs, the indistinguishability of the bosons then lead to a phase transition where a macroscopic occupation of the lowest energy quantum state is obtained. The atoms in the ground state form the so called "condensate".

7

The temperature required to reach condensation for a gas of non interacting bosons in a harmonic trap can be derived as follows : the occupation of each quantum state i with energy ϵ_i is given by the Bose Einstein distribution, which in the grand canonical formalism is

$$n_i = \frac{1}{e^{\beta(\epsilon_i - \mu)} - 1} \quad \beta = \frac{1}{k_B T}$$

where μ is the chemical potential, the normalization condition then requires that

$$N = \sum_i \frac{1}{e^{\beta(\epsilon_i - \mu)} - 1} \tag{2.2}$$

we can compute the sum (2.2) by turning it into an integral which includes all the terms except the population in the ground $i = 0$ state. For an isotropic three dimensional harmonic trap with frequency ω this gives

$$N = \frac{1}{(\beta \hbar \omega)^2} g_3 \left(e^{\beta(\mu - \frac{3}{2} \hbar \omega)} \right) + N_c \tag{2.3}$$

where N_c is the population in the ground state and g_3 is the Riemann zeta function. Since $g_3(\eta) \leq 1.202$ for $\eta < 1$ we see that a macroscopic population in the ground state occurs at the condensation temperature of

$$T_c = \left(\frac{N}{1.202} \right) \frac{\hbar \omega}{k_B} \tag{2.4}$$

Note that for realistic cases $k_B T_c > \hbar \omega$ so the condensation phenomenon is not simply just a freezing out of all excited modes due to the lack of thermal energy. It is a consequence of the particles' indistinguishability which enhances the probability for macroscopic occupation of the ground state when the number of available states becomes comparable to the number of particles.

Real atoms of course do in fact interact with each other. For rubidium 87 that we work with, although inter-atomic interaction is relative weak however, their effect can not

be neglected in describing the behaviour of the BEC. The interaction between two atoms

at low energies can be described by a short ranged contact interaction of the form

$$U_{int} = \frac{4\pi\hbar^2 a}{m}\,\delta(\mathbf{r} - \mathbf{r'}) = U_0\,\delta(\mathbf{r} - \mathbf{r'}) \tag{2.5}$$

where $\mathbf{r}$ and $\mathbf{r'}$ are the co-ordinates of the two particles in the system and a is the s wave

scattering length that characterise the behaviour of the scattered wavefunction at large

separations. Only the $l = 0$ collision is of relevance at low energies since higher angular

momentum collisions has a centrifugal barrier $l(l+1)/r$ which the incident particles must

overcome. In the condensed state, all bosons are in the same single particle state $\phi(\mathbf{r})$ [1],

we can therefore write the wavefunction for the N particle system as

$$\Psi(\mathbf{r_1}, \mathbf{r_2}, \cdots, \mathbf{r_N}) = \Pi_{i=1}^{N}\phi(\mathbf{r_i}) \qquad \int |\phi(\mathbf{r})|^2\, d^3\mathbf{r} = 1 \tag{2.6}$$

We can calculate the mean energy of the system $\langle\Psi|\hat{H}|\Psi\rangle$ with respect to the Hamiltonian

$$\hat{H} = \sum_{i=1}^{N}\left[\frac{\mathbf{p_i}^2}{2m} + V_{trap}(\mathbf{r}_i)\right] + U_0\sum_{i<j}\delta(\mathbf{r}_i - \mathbf{r}_j) \tag{2.7}$$

where $V_{trap}(\mathbf{r})$ is an external trapping potential

$$\langle\hat{H}\rangle = N\int\left[-\frac{\hbar^2}{2m}\phi^*\nabla^2\phi + V_{trap}|\phi|^2\right]\,d^3\mathbf{r} + \frac{N(N-1)}{2}U_0\int|\phi|^4 d^3\mathbf{r} \tag{2.8}$$

After minimizing (2.8) with respect to ϕ subjected to the normalisation constraint we derive

the equation of motion for the single particle wavefunction. It is customary to use a dif-

ferent normalization from (2.6) and define the condensate wavefunction as $\psi = \sqrt{N}\phi$ with

$\int|\psi(\mathbf{r})|^2 d^3\mathbf{r} = N$. The equation of motion for the condensate wavefunction (also called

Gross Pitaevskii equation) is [51, 52]

$$-\frac{\hbar^2}{2m}\nabla^2\psi + V_{trap}(\mathbf{r})\psi + U_0|\psi|^2\psi = \mu\psi \tag{2.9}$$

---

[1]This is not exactly true since for interacting particles, one of the effects of interaction is to create two correlated but uncondensed atoms out of two condensed atoms. This effect is called quantum depletion and is usually of order 4% or less in ^{87}Rb.

2.2   Two Dimensional Condensate

Of particular relevance to our experiment is the case of a two dimensional condensates. It is a long proven fact that condensation does not exist in a uniform 2D gas at finite temperatures due to the proliferation of long wavelength thermal fluctuations (this was encapsulated by the Mermin Wagner theorem) [32, 33]. However, the presence of a finite size confinement restrict the maximal wavelength of thermal fluctuations allowed and condensation will appear again. We can follow the same reasoning as used in the previous section to derive the condensation temperature of a two dimensional harmonically trapped gas of isotropic frequency ω

$$T_c = \frac{\hbar\omega}{\pi k_B} \sqrt{6N} \tag{2.10}$$

with condensate fraction

$$\frac{N_c}{N} = 1 - \left(\frac{T}{T_c}\right)^2 \tag{2.11}$$

To reach an effectively two dimensional regime, it is necessary to suppress dynamics in the third direction. We achieve this by restricting the tight direction to only zero point oscillations. This occurs when the chemical potential and thermal energy is less than the harmonic oscillator energy of the removed axis $\hbar\omega_z$

$$\mu, k_B T < \hbar\omega_z$$

When this is accomplished, we can take the ansatz for the condensate wavefunction as the product of a two dimensional condensate wavefunction and a harmonic oscillator ground state wavefunction in the frozen z direction

$$\psi(\mathbf{r}) = \Phi(x,y) \left(\frac{m\omega_z}{\pi\hbar}\right)^{1/4} e^{-\frac{m\omega_z}{2\hbar}z^2} \tag{2.12}$$

We can substitute the ansatz (2.12) into equation (2.9) to derive the two dimensional version of the Gross Pitaevskii equation. In the experimentally relevant regime of
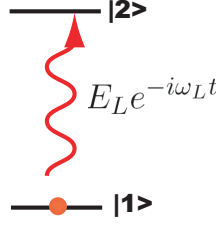
Figure 2.1: Two level atoms driven by a classical laser field of frequency ω_L. The bare atom has resonance frequency of ω_{12}.

$l_z = \sqrt{h/m\omega_z} > a$ where atomic collisions is still three dimensional, the result is

$$\left[-\frac{\hbar^2}{2m}\left(\frac{\partial^2}{\partial x^2} + \frac{\partial^2}{\partial y^2}\right) + \frac{m}{2}(\omega_x^2 x^2 + \omega_y^2 y^2) + U_0\sqrt{\frac{m\omega_z}{2\pi\hbar}}|\Phi|^2\right]\Phi = \left(\mu - \frac{\hbar\omega_z}{2}\right)\Phi \quad (2.13)$$

where we have substituted the case of a harmonic trapping in the remaining two dimensions.

In the limit of a large condensate, the kinetic energy term is negligible except near the boundary of the cloud, the transverse density is therefore given by the Thomas Fermi profile [34]

$$n(x,y) = \left[\frac{Nm\omega_x\omega_y}{\pi U_0\sqrt{\frac{m\omega_z}{2\pi\hbar}}}\right]^{1/2}\left[1 - \frac{x^2}{R_x^2} - \frac{y^2}{R_y^2}\right] \quad (2.14)$$

with the Thomas Fermi radii

$$R_x = \left[\frac{4NU_0\omega_y\sqrt{\frac{m\omega_z}{2\pi\hbar}}}{\pi m\omega_x^3}\right]^{1/4} \qquad R_y = \left[\frac{4NU_0\omega_x\sqrt{\frac{m\omega_z}{2\pi\hbar}}}{\pi m\omega_y^3}\right]^{1/4} \quad (2.15)$$

2.3 Atom Light Interaction

In this section we discuss the important interaction between light and atoms which allows us to manipulate and optically confine the atoms.

2.3.1   Steady State Solution To Optical Bloch Equation

Let us first consider the interaction of a single stationary two level atom driven by a classical monochromatic light field. The atom light interaction is given by the Hamiltonian

$$\mathcal{H}_{int} = -\hat{d} \cdot \hat{E} = -d(\sigma_+ + \sigma_-) \cdot (E_L e^{-i\omega_L t} + E_L^* e^{i\omega_L t}) \tag{2.16}$$

where d is the real dipole moment for the atom and E_L is the amplitude of the driving electric field. The raising and lowering operator for the two level atoms are $\sigma_+ = |2\rangle\langle 1|$, $\sigma_- = |1\rangle\langle 2|$.

In the rotating wave approximation, we retain only energy conserving terms in (2.16) and move to the frame evolving at the driving field's frequency ω_L. The net Hamiltonian for the driven atom system is

$$\mathcal{H}_{tot} = \hbar\delta\sigma_{ee} - \hbar(\Omega\,\sigma_+ + \Omega^*\sigma_-) \tag{2.17}$$

with $\delta = \omega_{12} - \omega_L$ is the detuning of the laser from the atom's resonance frequency and $\Omega = d \cdot E_L/\hbar$ the Rabi frequency characterizing the strength of the atom light interaction. The master equation of the system (which includes the decay of the excited atomic state due to the interaction with a vacuum reservoir)

$$\frac{d\rho_A}{dt} = \frac{1}{i\hbar}[\mathcal{H}_{tot}, \rho] + \gamma(\sigma_-\rho\sigma_+ - \frac{1}{2}\sigma_+\sigma_-\rho - \frac{1}{2}\rho\sigma_+\sigma_-) = 0 \tag{2.18}$$

allows us to compute the steady state solution of the density matrix for the atom. The coherence of the two level atom is characterised by the off diagonal elements of the density matrix

$$\rho_{21} = \frac{i\Omega}{\gamma/2 + i\delta}\left(\frac{\gamma}{\gamma + 2R}\right) \tag{2.19}$$

and the excited state population as

$$\rho_{22} = \frac{R}{\gamma + 2R} \tag{2.20}$$

with the optical pumping rate

$$R = \frac{\gamma|\Omega|^2}{\gamma^2/4 + \delta^2}$$

2.3.2 Moving Atom in a Light Field

In the next step, let us consider the interaction of a moving atom of momentum $\mathbf{p}$ with a light field. Description of the atomic states must now account for the atom's motional degrees of freedom so that our Hamiltonian for the atom light interaction is

$$\mathcal{H}_{tot} = -\hbar\Omega(r)\int |2,\mathbf{p}+\hbar\mathbf{k}\rangle\langle 1,\mathbf{p}|\ d\mathbf{p} - \hbar\Omega^*(r)\int |1,\mathbf{p}\rangle\langle 2,\mathbf{p}+\hbar\mathbf{k}|\ d\mathbf{p} \qquad (2.21)$$

since each photon absorption event must necessitate a momentum change by an amount equal to the momentum of a single photon $\hbar\mathbf{k}$.

Note that now, owing to the contribution from the kinetic energy of the atom, the resonance frequency for the transition $|1,\mathbf{p}\rangle \to |2,\mathbf{p}+\hbar\mathbf{k}\rangle$ is shifted from the bare resonance of a stationary atom to

$$\hbar\omega_{res} = \hbar\omega_{21} + \hbar\mathbf{k}\cdot\mathbf{v} + \frac{\hbar^2 k^2}{2m} \qquad (2.22)$$

The first term on the right hand side is the bare resonance energy for a stationary atom. The second is energy shift due to doppler effect, whilst the third term is the recoil energy which is generally much smaller (300 nK) than the others and is only of relevance at very low temperatures. The doppler term features importantly in the initial steps of laser cooling. By using a light that is of lower frequency than the atom's resonance, we can bring it into resonance with the atoms that satisfies $\mathbf{k}\cdot\mathbf{v} < 0$. Allowing the atoms to preferentially absorb photons moving opposite to the atom's motion.

The interaction with the light field induces a force on the atom given by

$$\langle\mathbf{F}\rangle = \frac{1}{i\hbar}\langle[\mathbf{p},\mathcal{H}_{tot}]\rangle = \hbar\nabla(\Omega\rho_{12}) + \hbar\nabla(\Omega^*\rho_{21})$$

Writing $\Omega = |\Omega|e^{i\phi}$ and using the steady state solution for the atomic coherences above

$$\langle \mathbf{F} \rangle = \hbar(\nabla|\Omega|^2) \frac{\delta}{\frac{\gamma^2}{4} + \delta^2} \left(\frac{\gamma}{\gamma + 2R} \right) + \hbar|\Omega|^2 \, (\nabla\phi) \, \frac{\gamma}{\frac{\gamma^2}{4} + \delta^2} \frac{\gamma}{\gamma + 2R} \qquad (2.23)$$

We see that the force contains two contributions : the first term, occurs due to a gradient in the intensity of the light field and dominates for large detunings when very little atomic excitation is created. We can interpret this as arising from the spatially varying AC stark shift of the ground state due to the light field. The second term, characterise the dissipative force due to photon absorption which dominates at low detunings. Since upon each absorption event, the atom receives a momentum kick of $\hbar\mathbf{k}$, and subsequent spontaneous emission event occurs in all directions so therefore impart zero momentum transfer onto the atoms on average. Therefore each spontaneous emission event delivers a momentum kick of $\hbar\mathbf{k}$ to the atoms.

2.3.3   Interaction With Real Atoms

In this work, we are mainly concerned with the force arising from the conservative interaction of (2.23) as it provides the least amount of disturbance to the atoms. In the limit of large detuning $\delta \gg \gamma, \Omega$ we can write this term as the gradient of a dipole potential

$$V = -\frac{\hbar|\Omega|^2 \, \delta}{\delta^2 + \frac{\gamma^2}{4}}$$

which is in fact the AC stark shift of the ground state in the presence of the light field. Heuristically, the oscillating electric field of the light induces an oscillating dipole moment in the atom which then interact with the light field to produce this energy shift. For real atoms, like ^{87}Rb, with many sub-levels, the light's interaction with each transition must be accounted for. But for detunings larger than the hyperfine splitting of the excited state we can simplify the interaction to that of the two D lines [53]

$$V_{dipole}(\mathbf{r}) = \frac{\pi c^2 \gamma}{2\omega_0^3} \left(\frac{2 + \mathcal{P}g_F m_F}{\Delta_{2,F}} + \frac{1 - \mathcal{P}g_F m_F}{\Delta_{1,F}} \right) I(\mathbf{r}) \qquad (2.24)$$

Here $\mathcal{P} = \pm1, 0$ for $\sigma_\pm$ and linearly polarized light respectively. g_F, m_F are the magnetic quantum numbers of the relevant ground states and $\Delta_{2,F}$, $\Delta_{1,F}$ are the detunings of the laser light from the D1 and D2 transitions respectively.

2.4 Gaussian Beam Dipole Trap

From equation (2.24), we see that it is possible to generate trapping potentials for the atoms using spatially varying intensity in the light field. A simple application of this is the confinement produced by a red detuned beam with a Gaussian profile $I(x, y) = I_0 e^{-2(x^2+y^2)/w^2}$ where w is the waist of the beam and the light is traveling along the z axis. For red detuning ($\Delta_{2,F}$, $\Delta_{1,F} < 0$)) the atoms are attracted towards intensity maximums. Hence by simply shining this Gaussian beam onto the atoms, one can create a confining potential in the x,y plane with atoms trapped at the center of the Gaussian profile. If the extent of the cloud is much smaller than the waist of the beam, we can Taylor expand to second order about the trap location to get

$$V_{Gauss}(\mathbf{r}) = \frac{\pi c^2 \gamma}{2\omega_0^3} \left(\frac{2 + \mathcal{P}g_F m_F}{\Delta_{2,F}} + \frac{1 - \mathcal{P}g_F m_F}{\Delta_{1,F}} \right) I_0 \left(1 - \frac{2(x^2 + y^2)}{w^2} \right)$$

so the gaussian beam produces a harmonic confinement in the x,y plane with trapping frequency proportional to $\sqrt{I_0/w^2}$

Chapter 3

Single Atom Imaging

This chapter explains the principles behind our imaging system and elucidate how we operate it to achieve high spatial resolution detection of atoms.

3.1 Imaging System

The center piece of the experiment, or the microscope part of the "Quantum Gas Microscope", is a specially designed imaging system, optimized for near diffraction limited resolution at 780nm. The schematics of the imaging system is shown in Figure 3.1, which consists of three parts. A custom made microscope objective positioned outside of the vacuum chamber, a plane parallel glass plate corresponding to the top face of the glass cell and a hemispherical surface inside the vacuum chamber. In order to achieve diffraction limited resolution, all three elements must be positioned relative to each other in pre-optimized positions. It is for this reason, that the mechanical mounting of both the objective and the hemisphere is designed in such a way that their orientation and position is completely defined by the top surface of the glass cell.

The first piece to be assembled, is the hemisphere shown in Figure 3.2. The
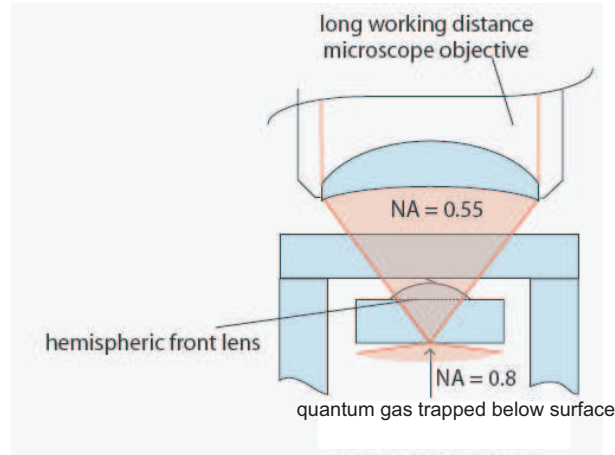
16

Figure 3.1: Schematics of the imaging system. A custom made objective sits outside of the vacuum chamber and forms a high resolution microscope together with the plane parallel glass plate of the glass cell surface and the hemispherical surface positioned inside the vacuum chamber
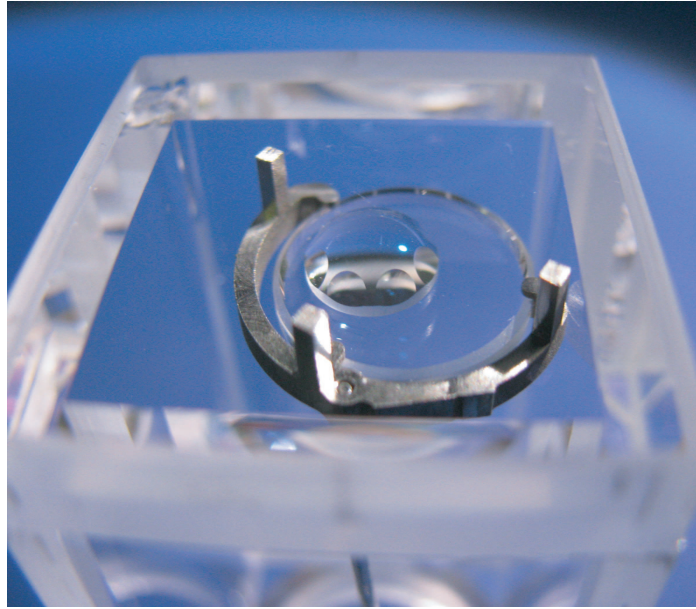

Figure 3.2: Photograph of hemisphere inside the glass cell. The hemisphere is optically contacted to a super-polished substrate surface that is held inside a stainless steel holder. The holder contains three prongs that pushes again the glass cell and define the position of the hemisphere relative to the glass cell surface.

hemispherical surface has 8 facets positioned at equal angular spacing. Their purpose is to prevent direct retro-reflection of beams incident on the center of the hemisphere which can otherwise lead to unwanted disturbances to the formed dipole potentials. The hemisphere is completed by optical contacting to a superpolished substrate which ensures that the glass surface facing the atoms is flat to within 1 angstrom, so that the atoms do not experience any potential disturbances due to surface effects. The entire construction is then clamped within a stainless steel holder with three prongs that pushes against the glass cell surface to position the tip of the hemisphere at a distance of 1.6mm below the inside of the glass cell. We then position the microscope objective (outside of the vacuum chamber) such that its optical axis coincide with the hemisphere center and is orthogonal to the glass cell surface. This was accomplished using a fizeau interferometer. We image the interference pattern of a large beam that traverses the imaging system twice upon reflecting from the flat surface of the hemisphere [1], with a reference wavefront obtained by reflection from a high quality glass surface . As shown in Figure 3.3, the interference patterns give us the capability to diagnose misalignments due to tilt, decentering or defocusing of the objective relative to the remaining pieces as they each give rise to distinctive wavefront aberrations. We then secure the objective to the glass cell via epoxy while monitoring the interferogram as the glue dries to prevent significant position shift as the epoxy cures.

In order to utilise the high spatial resolution, we must position the atoms close to the hemispherical surface. That this is necessary could be understood from the diagram shown in Figure 3.4. The presence of a nearby medium with refractive index greater than one, effectively increases the cone angle of light emanating from the object plane that will be able to pass through the aperture stop but only for objects close to the glass surface.

---

[1]The microscope focuses a collimated beam to the back surface of the hemisphere and we use the reflection from that surface as a proxy for the wavefront at the focus as it is not directly accessible to us.
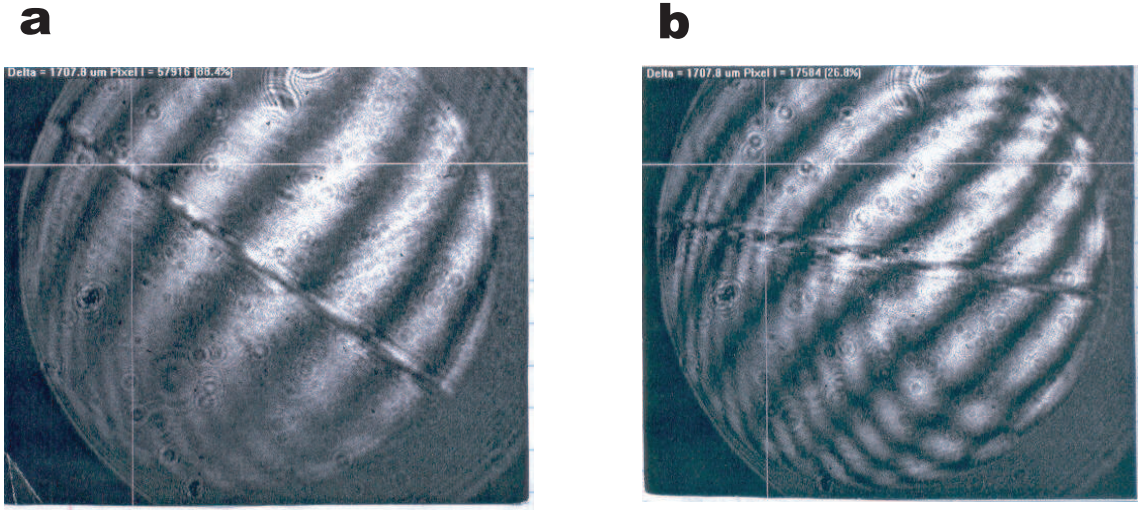
Figure 3.3: a. Fizeau interferogram of perfectly aligned objective showing the reflection from the flat surface has the wavefront of a plane wave. b. Interferogram of misaligned objective, the slight curvature in the fringes shows that the reflected wavefront deviates from a plane wave, most likely due to tilt of the objective optical axis with respect to the hemisphere center.

This is a commonly known technique of solid immersion microscopy [20] [2]. In the first version of our apparatus design, we operate with the atomic cloud at a distance of 1.5 μm below the glass surface. Subsequent investigation led us to abandon this configuration due to its close proximity to the glass surface and we now operate with the atoms positioned approximately 10 μm below the surface.

As well as placing the atoms close to the surface, we also compress the cloud greatly along the line of sight of the objective such that there is no relevant dynamics occurring along this axis. This is advantageous for two reasons. One, as this axis is invisible to the microscope, we would have to install imaging along another axis in order to reconstruct the

---

[2]An alternative explanation is that the wavelength of light is reduced by a factor of n equal to the refractive index of the dense material, hence the Rayleigh criteria gives a smaller resolution than in air by a factor of n
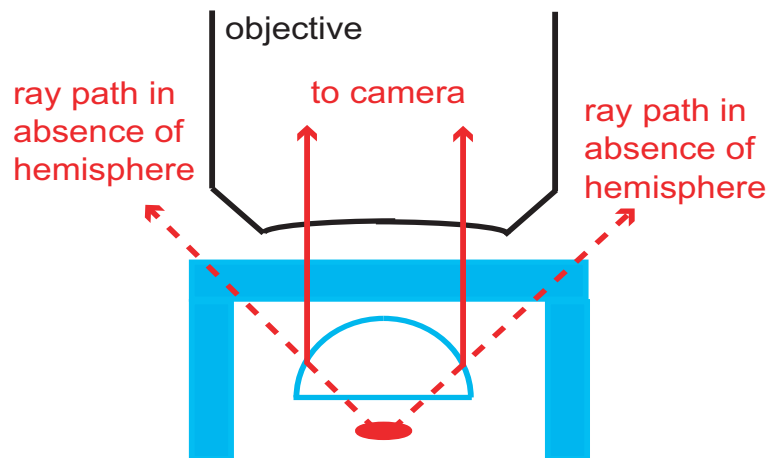
Figure 3.4: Schematics depicting the enhancement of numerical aperture in solid immersion microscopy. In the absence of the nearby hemisphere, the large angled emission from the atoms would not be collected by the objective (shown in dashed red line). In the presence of the hemisphere, these rays undergo refraction at the hemisphere which redirects them into the objective (solid red line)

dynamics in this third dimension [3]. Secondly, the objective has a finite depth of focus of 1.2 μm therefore images will be obscured by any signals outside of the diffraction limited region. It is for these reasons that we construct a two dimensional optical trap for the atoms just below the surface as described in Chapter 4.

Note that although much care was taken to ensure that the objective is positioned correctly for aberration free wavefront, this need not in fact be necessary, since after gluing, any aberration is likely to be static. Provided that the exact wavefront at the focus could be reconstructed, the aberrations could in principle be fully corrected for by the insertion of an appropriately manufactured phase plate with the conjugated phase distortion, hence restoring the high resolution.

Wavefront reconstruction is generally difficult however, especially when we could

---

[3]This is not necessary for systems contains certain symmetry where it is possible to reconstruct the full image from a projected image, for example the use of inverse Abel transform for axially symmetric condensate in [35]
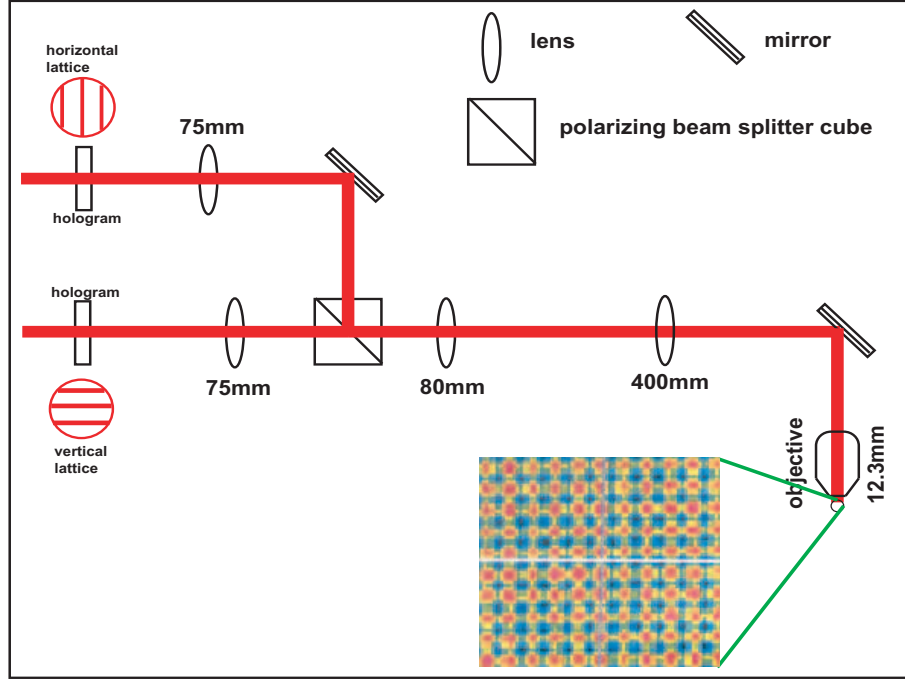
Figure 3.5: Projections optics for pinning lattice. Two orthogonally oriented 1D lattices are combined on a polarizing beam splitter cube and sent through the remaining 4f imaging system including the microscope objective to form a square lattice at the atoms.

not access directly the other side of the imaging system. Since aberrations due to misalignment of the objective are likely to be random in nature and could not be computed from first principle, this method of reaching diffraction limit is unlikely to be successful.

Nevertheless, phase conjugation was still useful for us, in circumstances where the aberration arose from a known cause and could be computed. Such was the case when it became necessary for us to move the atom trap further away from the superpolished surface. In order to maintain diffraction limited imaging with the atoms 10 μm away, the imaging process was simulated using the ray tracing program Oslo, from which the wavefront aberration could be computed and the appropriate phase conjugation plate manufactured.

3.2   Imaging Procedure

Once the imaging system is set up, we may use it to take high quality fluorescence images of the atoms. The imaging process consists of the following sequence of events (see Figure 3.6) in the order which they occur :

1. The atoms are first localized for the duration of the imaging process. We do this by imposing a deep square lattice potential in the plane of the atoms with depth of up to 340 μK. We generate the square lattice pattern by shining 795 nm light 50 GHz to the blue of the rubidium D1 line, on two static transmission phase holograms with orthogonally oriented line patterns as shown in Figure 3.5. We then combine the two patterns on a polarizing beam splitter cube to form a square lattice. This pattern is then projected onto the atoms using two 4f imaging systems with the microscope as the last "lens". The resultant lattice pattern has a lattice spacing of 620 nm after a factor of 0.031 in magnification. Because the lattice pattern is merely an image of the hologram pattern, the structure (i.e. lattice spacing) is independent of the wavelength of light used. Therefore we can use the same imaging path both for projecting far detuned lattice patterns (for doing many body experiment) as well as near resonant ones here as in the pinning lattice. We also impose a deep potential in the vertical direction (about 1 mK) by using the same laser and creating a lattice in the vertical direction similar to the way vertical confinement for our two dimensional quantum gas was made (see section 4.4).

2. After the pinning lattice has reached full power, all previous confinement of the atoms, optical and magnetic are switched off. We also switch on currents through three large coils made using ribbon cables that nulls the magnetic field at the location of the atoms, which is necessary for the next step of the experiment.

3. Two molasses beams with co-propagating repump, 80 MHz to the red of the imaging transition $F = 2, m_F = 2 \rightarrow F' = 3, m'_F = 3'$ are switched on. These serves two purposes: one, the polarization of the molasses are adjusted to give rise to polarization gradient cooling effects [54]. Here polarizations of the pinning lattice beams are important to allow effective operation of the molasses beam, since any nonlinear polarization of the beam effectively generates a vector light shift which mimics a magnetic field. The lattice beams has been carefully aligned to attain as close to linear polarization as possible. The second purpose of the molasses beams are to cause the atoms to scatter 780nm photons which are then collected by the microscope and constitute fluorescence signal of the atoms.

4. After waiting 50 ms for the transients of the molasses to disappear, the camera shutter opens and collect signal for typically 1s. Figure 3.7 shows a typical image of atoms released from the two dimensional surface trap.

A histogram of our images always shows two peaks corresponding to the absence and presence of an atom. We believe the absence of other peaks signifying site occupation greater than one is due to the occurrence of light assisted exothermic molecule formation between two closely spaced atoms which occurs in multiply occupied sites [55]. This removes all sites occupied by even number of atoms and reduce sites with odd occupation to a single atom. So our detection mechanism measures only parity of atom number per site.

3.3   Image Analysis

The fluorescence images of the atom allows us to directly measure the point spread function of our imaging system (or response to an impulse, here being the point object of an atom). This was done by taking several pictures with very sparse atom distribution. We
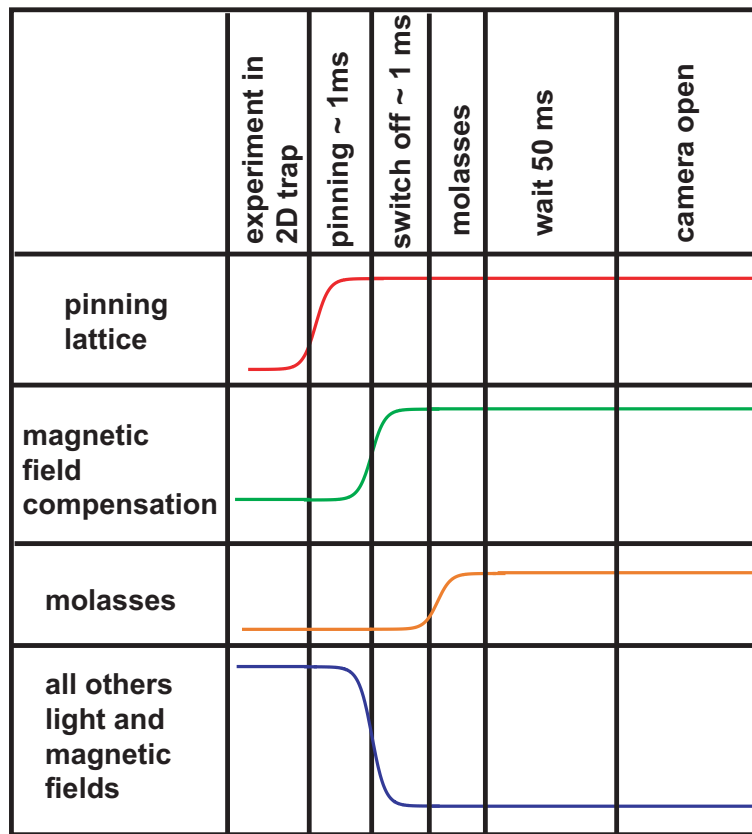
Figure 3.6: Sequence of events for fluorescence imaging of atoms.
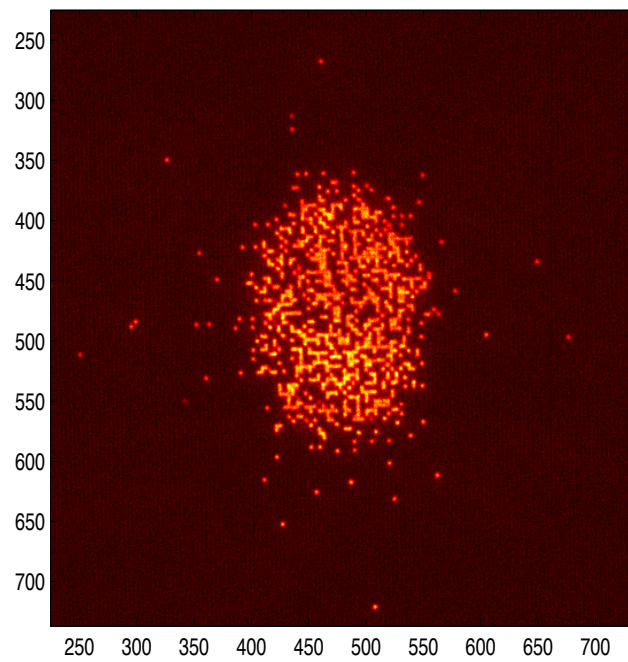
Figure 3.7: Fluorescence image of atoms released from surface trap 10 μm away from the surface.
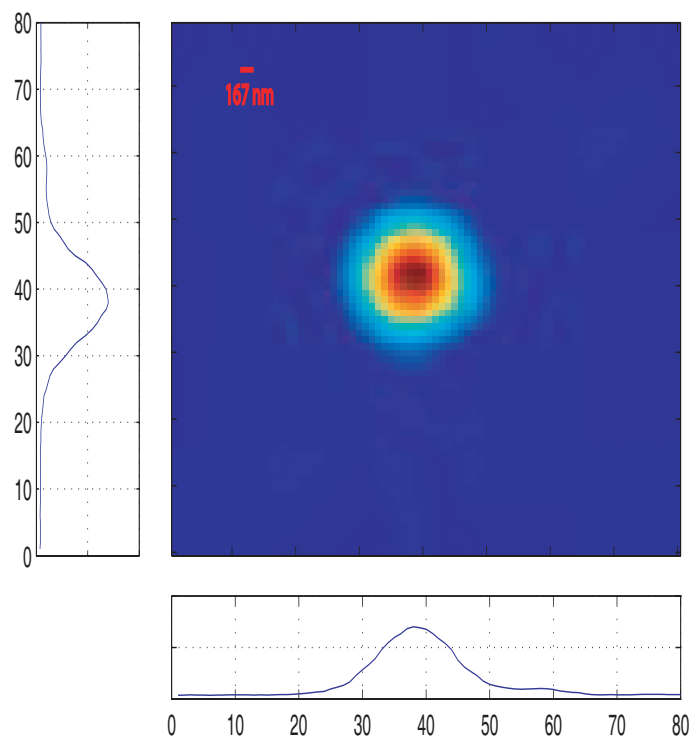
Figure 3.8: Point spread function of imaging system.

visually identify the locations of isolated atoms in each image, then overlap the peaks of each single atom intensity profile in order to compute an averaged intensity profile of a single atom. The resultant pattern is then fitted with a two dimensional gaussian. Figure 3.8 shows the result of the point spread function computed this way from fluorescence images of atoms at about 10 μm below the surface. Knowing the magnification of the imaging system, the FWHM of the point spread function are 0.593 x 0.605 μm in the horizontal and vertical directions respectively.

The second type of analysis frequently performed on these images is to identify the location of the atoms in the image. Typically this was done by obtaining, prior to each experiment run, the point spread function as described above, and the lattice geometry by Fourier transform of some densely populated images. We then determine the location of atoms in each image by determining the least square multiple of the point spread function for the data at each lattice site. Fit values above a predetermined threshold indicate the presence of an atom.

For the sake of expediency, we also implement a faster algorithm using built in functions within Matlab's Image Processing Toolbox. By examining sparsely populated images, we identify the appropriate structuring elements characterizing the intensity profile of a single atom. This here serves the analogous purpose as the point spread function above and need only be determined once for a fixed camera focusing. We then perform morphological opening using this structuring element to probe the image we wish to examine. After subtracting this from the original image and performing a gamma correction, we obtain a high contrast version of the fluorescence image from which the location of the atoms could be easily obtained by searching for local maximums in intensity whose average neighborhood values exceed a threshold hold level that was determined by tests with images where manual identification was feasible. This allowed us to determine the atom number, center

and radii of cloud in less than 5s per typical image.

Chapter 4

Optical Surface Trap

In this chapter, we explain in detail, the setup of how we produce a two dimensional condensate in the experiment suitable for performing optical lattice experiments with the quantum gas microscope. Our current setup is a revised version of an older configuration [56] which suffers from surface effects due to adsorbed rubidium atoms on the superpolished substrate. We circumvent this problem by moving the atoms further away from the glass surface.

4.1 Old Apparatus Setup

The main components of our old setup is shown in Figure 4.1 [57]. We start the experiment by producing an almost pure condensate of Rubidium 87 in the F $= 1$ $m_F = 1$ hyperfine state in a magnetic trap of cigar geometry. In order to produce a two dimensional condensate close to the glass surface, we loosen the confinement in the transverse directions (orthogonal to gravity) by changing the magnetic field configuration to a spherical one and move the center of the magnetic trap 1.6mm into the glass surface. This squeezes the atoms against a repulsive potential at the surface formed by a blue detuned evanescent wave, thus
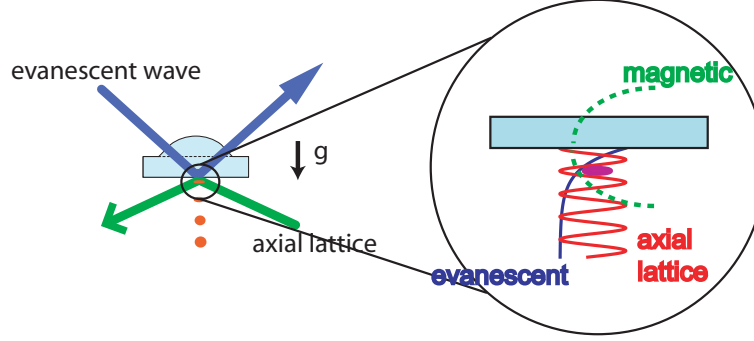
Figure 4.1: Schematics of our old surface trap setup. The magnetic field center is used to move the atoms towards the surface where they encounter a 765 nm evanescent wave incident from the curved side of the hemisphere and creates an exponentially decaying repelling potential that prevents the atoms from falling into the surface. The same laser is also used to power the axial lattice incident from the bottom of the hemisphere that creates a 1D lattice orthogonal to the glass surface. In the final stage, the atoms are loaded from the evanescent-magnetic combined trap to a single well of the axial lattice closest to the glass surface as shown on the right.

greatly increasing the vertical trap frequency, typically to about 800 Hz.

To further increase the vertical confinement, in order to reach deeper into the two dimensional regime, in the second stage we load the atoms into the first well closest to the glass surface of a vertical lattice potential produced by a blue detuned vertical standing wave. This one dimensional lattice is formed by the interference of a grazing incidence beam with its reflection from the flat surface of the hemisphere, with the angle of incidence tuned to give a lattice spacing of 1.5 μm. At this stage, we have a two dimensional condensate 1.5 μm below the superpolished substrate that forms the starting point of all subsequent experiments.

Although this configuration allowed us to utilise the high resolution of the microscope, there were severe limitations due to the close proximity to the glass surface. In detail, we encountered the following technical difficulties :

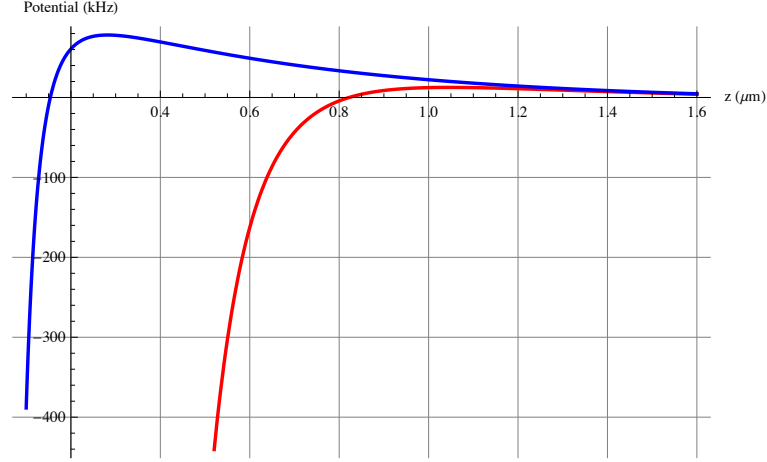- There is a slow leakage of atoms out of the evanescent wave trap towards the glass

Figure 4.2: Potential barrier from evanescent wave and Casimir Polder effect with the surface (blue curve), and the same potential added to electric field due to 10 million adsorbed rubidium atoms on the surface (red). The potential barrier to the surface is almost non existent after including the effects of the adsorbed atoms.

surface. When enough adsorbed rubidium atoms had accumulated at the surface, it created an attractive potential [1] that reduced the barrier to the surface created by the evanescent wave. One can estimate its effect roughly by using the measured electric field from adsorbed rubidium atoms on a glass surface obtained in [71]. We assume the distance dependence of the electric field is consistent with that of a point charge, as would be expected for atoms consistently deposited at the same location on the glass surface. Figure 4.2 shows the resultant potential barrier from the surface for 10 million adsorbed atoms on the surface in comparison to no adsorbed atoms, it is clear that the barrier due to the evanescent wave is rapidly washed away by the adsorbed atoms, making it extremely easy for atoms to tunnel to the surface. Note that the cycle rapidly becomes a run away process as adsorbed atoms leads to reduced barrier which then encourages even more atoms to get stuck to the surface. As a consequence

---

[1] Adsorbed atoms onto the surface changes its electronic structure leading to the valence electron residing partially inside the surface therefore creating a weak dipole. The effect is dependent on the work function of the surface and is not as severe for glass as it is for metallic surfaces.

we were not able to load the evanescent wave trap using the same location on the surface for longer than about three months.

- The surface impurity impedes our ability to precisely control the repulsive potential that keeps the atoms away from the surface, therefore we lack good control of atom number and temperature in the 2D trap. We also have no reliable method to reproducibly produce the small atom numbers (approximately 2000) needed to load the subsequent two dimensional optical lattice with one atom per lattice site.

- Impurities on the surface also cause an-isotropic expansion in the plane and sometimes even pin atoms to local spots. An example of this is shown in Figure 4.3 where the condensate is allowed to undergo free transverse expansion for 2 seconds within the axial lattice before fluorescence imaging. A significant number of atoms remained pinned to this location. This occurred despite of the fact that the atoms experienced a force parallel to the plane of the surface due to the tilt of the hemisphere axis with respect to gravity (about 0.6^o). One can use this to estimate roughly the sideways gradient in the plane due to the adsorbed atoms. In units of an equivalent magnetic field gradient, this translated to a gradient of 0.36 G/cm. The susceptibility to surface contaminants was a great impediment to our abilities to produce controlled known potentials for the atoms which is necessary when comparing to theory in optical lattice experiments.

It was for these reasons that we decided to modify our surface trap configuration. Our changes were implemented with two major objective :

- To reduce the effect of surface impurities, we will implement the two dimensional trap for the condensate at a distance of 10μm away from the glass surface. We deemed this distance to be large enough to provide immunity against surface impurities and

Figure 4.3: Fluorescence images of atoms after expansion in axial lattice for 2s. Signal shows atoms pinned by surface impurities.

adsorbed rubidium atoms whilst still allowing us to utilise the enhanced numerical aperture afforded by being close to the glass surface. We achieve this by replacing the evanescent wave trap with a vertical lattice of lattice spacing 10 μm and loading into the first well of this lattice after condensation in the cigar trap.

- RF evaporation does not allow us to reproducibly make small condensates as once the RF frequency gets below the chemical potential of the condensate we become susceptible to fluctuations in the magnetic field trap bottom (not actively stabilized). We therefore decided to control the atom number via optical means for which the stability is mainly determined by fluctuations in beam power (which is actively stabilised). Our final configuration utilizes a "dimple" trap, or a red detuned dipole beam of small trap volume, which we use to reduce our atom number beyond the stable operating point of RF evaporation without exuberant increase in temperature or loss in stabil-

ity. We then subsequently put the atoms into a large volume red dipole trap prior to loading into the optical lattice. This trap has a low trap depth (on order of nK) which we use to limit the temperature of the cloud. The powers in both beams are actively stabilized via the setup described in Appendix A. With the combination of both methods we can consistently produced condensates of approximately 1000 atoms with about 4 % fluctuation in atom number.

In the remainder of this chapter we will describe in detail, the setup and characteristics of our improved trapping scheme which will take us closer to working on many body physics.

4.2   The $10\mu m$ Lattice

In this section, we describe the $10\mu m$ lattice (also referred to as the big lattice) that is used as a bridge between the end of the usual BEC production and the two dimensional optical trap where we will eventually carry out the experiments with optical lattices.

The big lattice consists of a vertical lattice formed from the interference of an incident beam on the flat side of the hemisphere with its reflection (see Figure 4.4) from the glass surface. The light source for the lattice is the output of a titanium sapphire femtosecond laser (Coherent Mira). In order to transport the light from the laser table to the experiment table via single mode fiber without excessive spectral broadening due to nonlinear effects, we broaden the time width of the pulse as described in appendix B with a pair of matched gratings. The resultant light at the fiber output has an autocorrelation full width half maximum of $153\mu m$ and center wavelength of 757.4nm.

In order to generate a lattice spacing of about $10\mu m$, the incident beam must impinge upon the surface at a very shallow angle of about 2° to the glass surface. At this
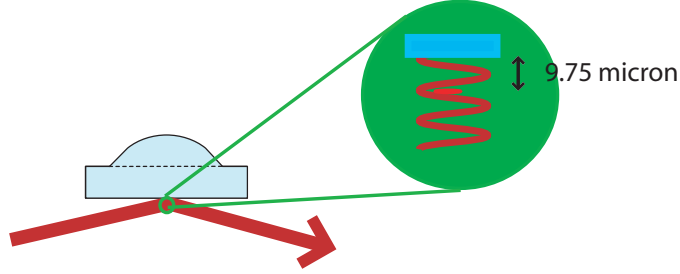
Figure 4.4: Geometry of the big lattice beam. The incident beam from the left side interfere with the reflection from the surface to form a one dimensional lattice in the vertical direction. We load the atoms into the first well of this lattice.

small angle, a circular incident beam would result in a highly elliptical cross section in the transverse plane, therefore we shape the incident beam to an aspect ratio of 2.6 : 1 with cylindrical lenses as shown in Figure 4.5. A higher aspect ratio of 28.7:1 would be required to generate a truly circular cross section at the atoms, but such a high aspect ratio would necessitate that one axis of the beam having a very small waist and hence a very short Rayleigh length. The rapid divergence would likely lead to clipping upon entering the glass cell. In any case, at the point of loading into the big lattice, the transverse confinement is still dominated by the magnetic trap, therefore the precise geometry of the big lattice beam is not so important.

In Figure 4.5, we illustrate the sequence of optical elements used to generate and image the big lattice beam onto the atoms. A motorized mirror is placed at the object plane of the two lens imaging system whose image point is at the atoms. When rightly focussed, this allows us to change the beam's angle of incidence via rotation of this mirror with minimal shift in beam position. A 30mm thick plane parallel glass plate is used to change the beam position in the object plane and allows us to center the beam onto the atoms.
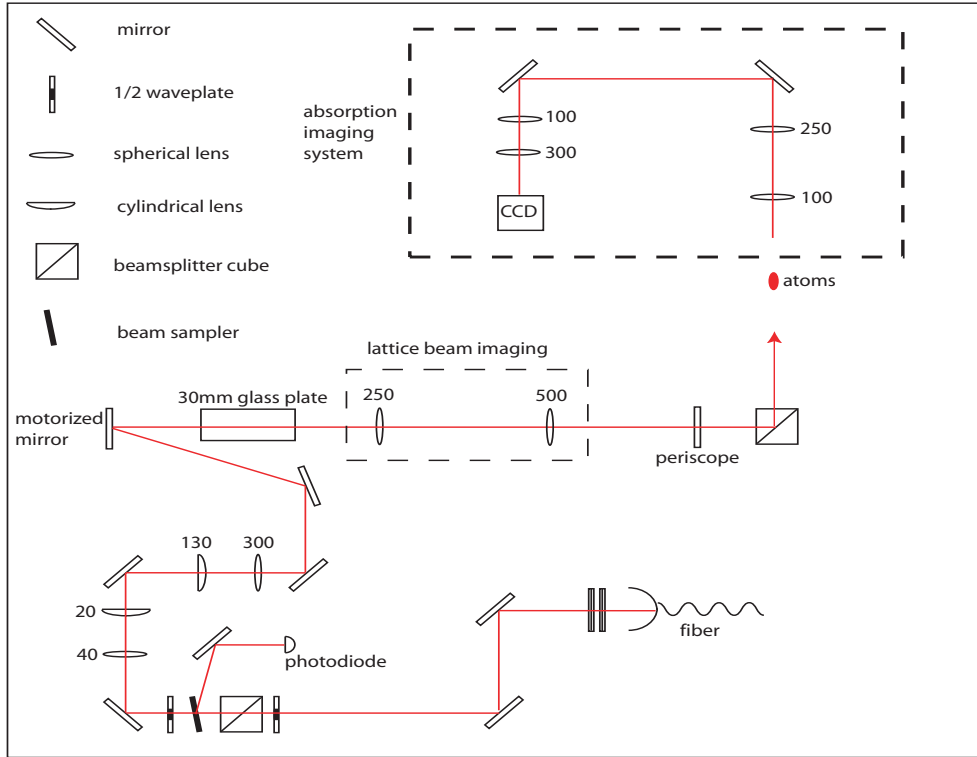
Figure 4.5: Optics setup for the $10\mu m$ lattice. The two lenses in the lattice beam imaging system image the beam position and angle in the object plane (equal to location of the motorized mirror) onto the atoms. The atom absorption imaging system in the upper right hand corner is used to align the lattice beam to the correct location with respect to the atoms

Figure 4.6: Absorption image of the atoms using 780 imaging light passing through the same fiber as the big lattice beam

To position the beam onto the atoms, we pass 780nm imaging light through the same fiber as the big lattice and use it for absorption imaging via the imaging system shown in the upper right hand corner of Figure 4.5. When correctly placed, we see two symmetrically placed images of the atom cloud (the atom's shadow and its reflection in the glass surface) as shown in Figure 4.6.

In order to measure approximately the lattice spacing of the big lattice, we move the atoms by shifting the minimum of the cigar trap to varying vertical distances below the surface then ramp up the big lattice to full power over 200ms. After holding the atoms in the lattice for 10ms, we do absorption imaging after 10ms time of flight and use a gaussian fit to find the center position of the cloud. The vertical position of the cloud (see Figure 4.7) shows plateaus corresponding to loading into the first, second and third well of the big lattice. This way, we deduce the lattice spacing is approximately $9.75\mu m$.

In order to load the atoms into the big lattice without significant heating or loss, it is necessary to circumvent the high density which results as an increase in the vertical trap frequency from the 140 Hz in the cigar configuration to the 0.9 kHz in the big lattice. To achieve this, we loosen the transverse confinement by converting from a cigar trap to a spherical configuration at the point when the big lattice power is sufficient to prevent
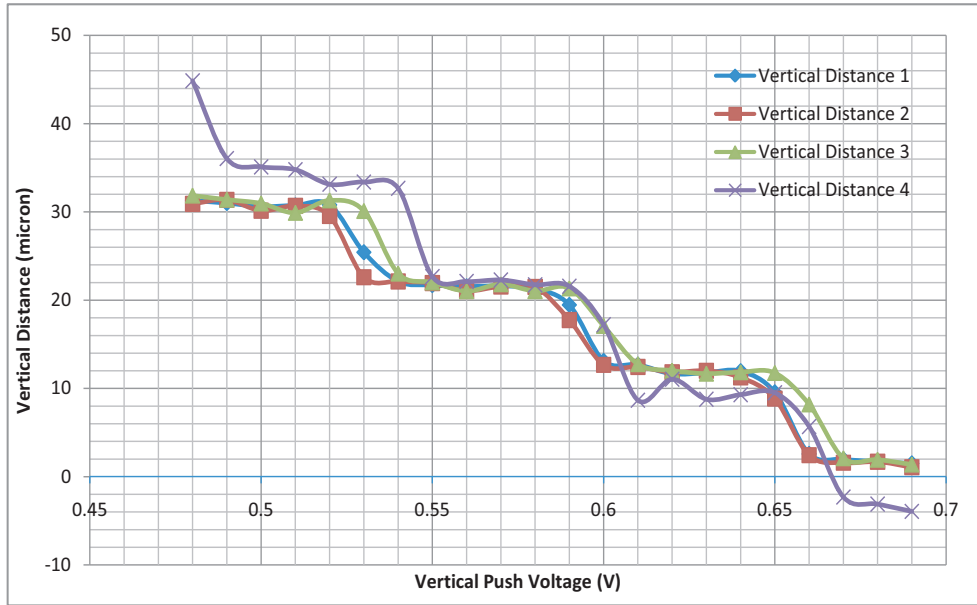
Figure 4.7: Measurement of approximate lattice spacing. The cigar trap center is moved to varying distances below the surface by changing the voltage supplied to a push coil (a higher voltage is closer to the surface). After pushing to desired location, the big lattice is ramped up to full power in 200ms. The atoms are imaged after 10ms hold time in the lattice and 10ms time of flight. We use a gaussian fit to deduce the center of the cloud for each distance. The four lines represents the same experiment taken on different days over a space of one week which shows that our loading distance remains roughly stable over time.

sagging due to gravity. After full conversion to a spherical trap, the big lattice is then ramped up to maximum power. Our optimized parameters gives a loading efficiency of 78 % into the big lattice with a vertical confinement of 0.95 kHz as measured from parametric heating.

4.3   Dimple Trap

The next stage in the surface trap sequence is the loading of atoms into the red detuned dimple trap. As mentioned previously, the use of the dimple allowed us to reach lower atom numbers and also freed us from the necessity of a magnetic trap (this would be important for experiment involving atoms in differing magnetic states). In this section, we describe the rationale behind its use and how it was implemented.

Previous works on the dimple trap has concentrated on its ability to increase phase space density by modifying the geometry of the trapping potential. The fact that this is possible could be seen readily from thermodynamic relations. Let us consider an ensemble of N thermal atoms subject to a spatially varying trapping potential of the form $U(\mathbf{r})$ where the potential minimum at $\mathbf{r}_{min}$ satisfies $U(\mathbf{r}_{min}) = 0$. The atoms will distribute themselves in a spatial pattern given by the Boltzmann distribution, where the spatial density is

$$n(\mathbf{r}) = n_{peak} \, e^{-\frac{U(\mathbf{r})}{k_B T}} d^3 \mathbf{r}$$

and the normalisation condition

$$N = n_{peak} \int e^{-\frac{U(\mathbf{r})}{k_B T}} \, d^3 \mathbf{r} \tag{4.1}$$

From equation (4.1), we see that one may define an effective volume for the cloud as

$$V = \int e^{-\frac{U(\mathbf{r})}{k_B T}} \, d^3 \mathbf{r} \tag{4.2}$$

such that $n_{peak} = N/V$.

The Hamiltonian for the ensemble $H = \sum_{i=1}^{N} \frac{p_i^2}{2m} + U(\mathbf{r}_i)$ allows us to write the

partition function as

$$Z_N = \frac{1}{h^{3N} N!} \int e^{-\frac{H}{k_B T}} d^3\mathbf{p}_i \, d^3\mathbf{r}_i \tag{4.3}$$

$$= \frac{1}{\lambda_{dB}^3 N!} \left(\int e^{-\frac{U(\mathbf{r})}{k_B T}} d^3\mathbf{r} \right)^N = \frac{Z_1^N}{N!} \tag{4.4}$$

with the thermal de Broglie wavelength $\lambda_{dB} = \sqrt{\frac{h}{2\pi m k_B T}}$ and the single particle partition

function

$$Z_1 = \frac{1}{\lambda_{dB}^3} \int e^{-\frac{U(\mathbf{r})}{k_B T}} d^3\mathbf{r}$$

The entropy per particle in the cloud is related to the partition function via

$$\frac{S}{N} = \frac{1}{N} \frac{\partial}{\partial T} (k_B T \log Z_N) \tag{4.5}$$

$$= k_B \left(\frac{5}{2} + \frac{T}{V} \frac{\partial V}{\partial T} - \log(n_{peak} \lambda_{dB}^3) \right) \tag{4.6}$$

$$= k_B \left(\frac{5}{2} + \gamma - \log(n_{peak} \lambda_{dB}^3) \right) \tag{4.7}$$

where we assume that V has a the functional dependence on temperature as $V \propto T^\gamma$.

From equation (4.6) we see that in an adiabatic operation that conserves the total

number of particles (hence constant entropy per particle) one has the possibility of greatly

increasing the phase space density $n_{peak} \lambda_{dB}^3$ by changing the parameter γ. But this could

not be accomplished simply by a change in the strength of the potential ($U(\mathbf{r}) \rightarrow KU(\mathbf{r})$)

as this corresponds only to a scaling of the temperature so that the volume changes as

$V \propto (T/K)^\gamma$ without a change in the γ parameter. However γ could be modified by a

change in the functional form of the trapping potential. In Figure 4.8, we illustrate some

sample potentials with their respective γ. Realisation of increasing the phase space density

this way was first achieved by Pinkse *et. al.* [1] with spin polarized atomic hydrogen where

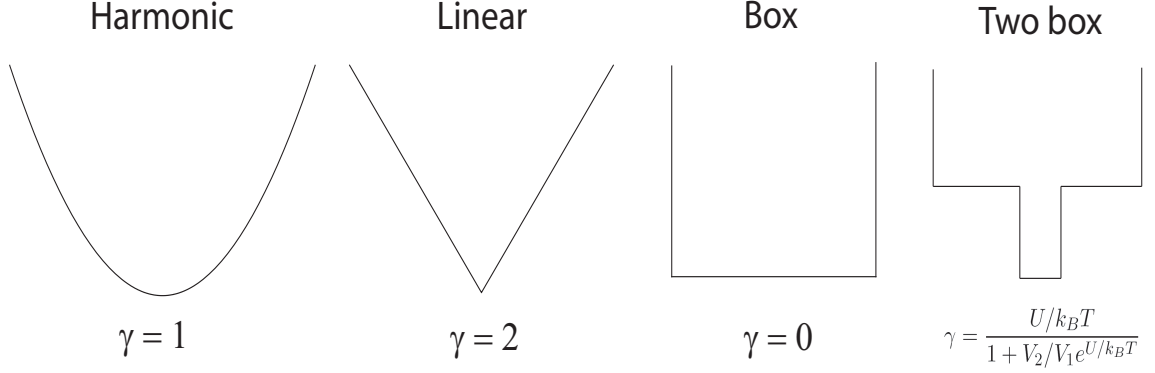a deformation of the magnetic trap from harmonic to nearly linear gave rise to an increase

Figure 4.8: γ for some simple trapping potentials in two dimensions.

in phase space density by a factor of 2. It was also utilised in later experiments on all optical production of Bose Einstein condensation [4].

A more general type of deformation is illustrated in Figure 4.8, the two box potential. This was first implemented by Stamper-Kurn *et. al.* in [3] and later in [2]. Such a configuration is easier to achieve experimentally as it could be accomplished by simply superimposing two potentials of different depths and sizes. In the case of [3], this was accomplished by a tightly focussed optical trap combined with a large volume magnetic trap. In the Cs experiment of [2], this was done using two different sized dipole traps. Our approach uses a combination of the above two methods.

We extend the original idea of [3] by considering an extension of the "two-box" model illustrated in Figure 4.9. N particles are originally confined in a box potential of volume $V_0 = V_1 + V_2$ with initial temperature T_0, density n_0 and phase space density Γ_0. The potential within a subvolume V_2 of the box is then lowered adiabatically by an amount U to form a "dimple" so that the peak density in the dimple exceeds that of the reservoir by an amount $e^{U/k_B T}$ and the ensemble equilibrates to a higher temperature T_2 with phase space density Γ_2 within V_2.
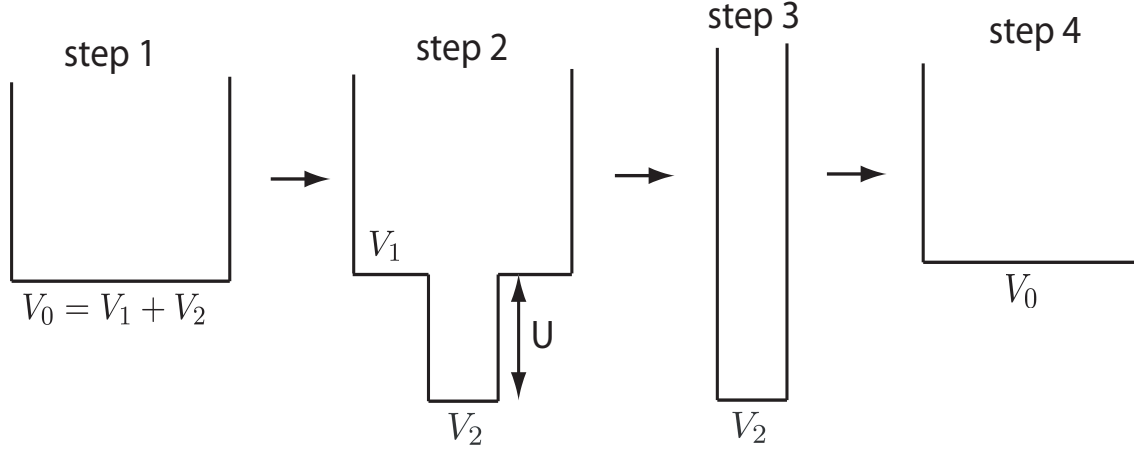
Figure 4.9: Sequence for cooling using the dimple trap with the two box model. An ensemble of N atoms is initially held in a box potential of volume V. In step 2, a dimple trap of volume V_2 and depth U is superimposed on top of the box potential. In step 3, the reservoir atoms in volume V_1 are released leaving the remaining atoms to equilibrate in V_2. In step 4, the box is adiabatically expanded back to volume V_0

The application of equation (4.6) to equate the entropy per particle in steps 1 and 2 shows that the phase space density in V_2 will exceed the original phase space density by an amount

$$\log\left(\frac{\Gamma_2}{\Gamma_0}\right) = \frac{\frac{U}{k_B T_2}}{1 + \frac{V_2}{V_1} e^{\frac{U}{k_B T_2}}} \tag{4.8}$$

For $V_2 \ll V_1$ and $e^{U/k_B T_2} \ll V_1/V_2$ (potential not so deep as to encompass all the atoms) one can obtain an almost arbitrarily large increase in phase space density $\Gamma_2 = \Gamma_0 e^{U/k_B T_2}$ and give rise to condensation of atoms in V_2 as shown in [3]. But note that condensation was a local phenomenon here, as the dimple perturbs the eigenstates only locally. As shown in [3], the atoms in the reservoir remains thermal.

Next we consider utilising the local increase in phase space density in the following ways as shown in steps 3 and 4 of Figure 4.9. In step 3, we remove the reservoir atoms in a one step "evaporation" process and allow the atoms in the dimple to equilibrate afterwards. By computing the average energy per particle before and after the evaporation, the

equilibrium temperature in step 3 is [5, 6]

$$T_3 = T_2 \frac{1 + \frac{V_2}{V_1} e^{\frac{U}{k_B T_2}}}{1 + \frac{V_2}{V_1} e^{\frac{U}{k_B T_2}} + \frac{2U}{3k_B T_2}} \tag{4.9}$$

By letting the reservoir atoms escape carrying above the average kinetic energy per atom, the remaining smaller number of atoms equilibrate to a lower temperature. Note that one can also use this method to lower the atom number in a way that is more deterministic than RF evaporation since the final number of atoms retained depend only on the initial density (which is weakly dependent on the total atom number) and the properties of the dimple beam. The proportion of atoms retained is

$$p = \frac{\frac{V_2}{V_1} e^{\frac{U}{k_B T_2}}}{1 + \frac{V_2}{V_1} e^{\frac{U}{k_B T_2}}} \tag{4.10}$$

In step 4, we expand V_2 adiabatically back to the original size V_0. Since phase space density is conserved and the density of atom is reduced by a factor of V_0/V_2, the final temperature of the atom is

$$T_4 = T_3 \left(\frac{V_2}{V_1 + V_2} \right)^{(2/3)}$$

In Figures 4.10 and 4.11, we show the final temperature and proportion of atoms remaining as a function of the dimple depth for various volumes and initial temperatures. Both final temperature and atom number are approximately linear functions of the dimple depth (proportional to dimple power here) in this region (this will not be true in the param- eter regimes of very high phase space density, or very low temperatures since the density in the dimple becomes constrained by three-body losses [7]) and that for a lower initial temperature, it becomes progressively harder to cool and still retain atoms since very low dimple depth are required and atom number declines more quickly with decreasing dimple depth at lower temperature. Note that although $V_2 \ll V_1$ is optimal for reaching lower tem- peratures, it also retains much less atoms which will be more susceptible to residue heating such as from spontaneous scattering from the dimple trap light, an effect not included here.
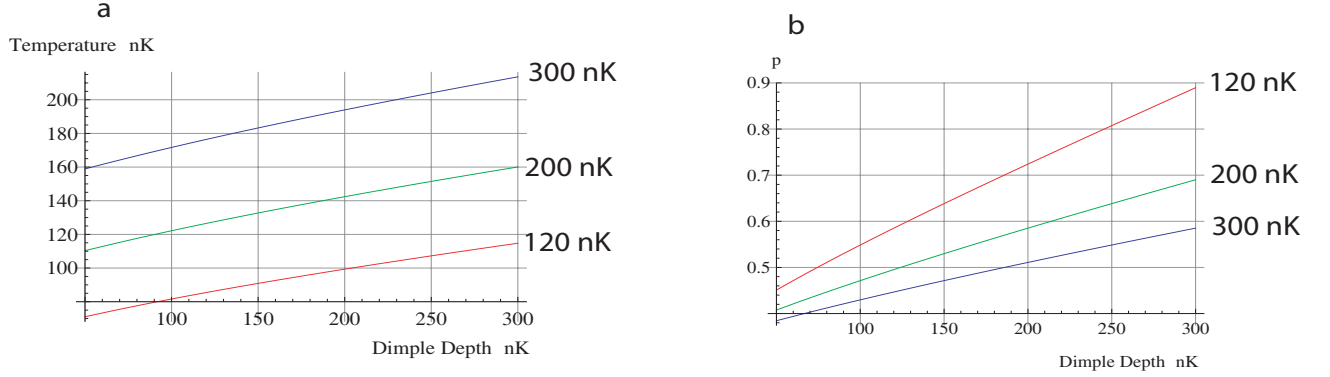
a

Temperature nK

b

Figure 4.10: Final temperature of dimple cooling (a) and proportion of atoms retained (b) as a function of dimple depth for various initial temperatures of the cloud as labeled on the graphs. $V_2/V_1 = 0.5$

Instead of expanding the dimple, one can also perform further evaporation in the dimple by lowing the depth as was done in [8]. Evaporation in the dimple can be very efficient for species with low inelastic decay rate, due to the high density which encourages thermalization.

4.3.1   Dimple Trap Setup

The dimple trap in our experiment serves two main purposes

1. Reproducibly make controllable small atom number clouds.

2. Prevent atom loss or shaking during magnetic field shut off.

We did not focus on the cooling aspect of the dimple as there are further stages subsequent to loading the dimple that would lead to temperature increase, although it is likely that some variant of the above mechanism is in operation. In future experiments, it may be possible to utilise the cooling properties of the dimple as well as the above two.

We create the dimple beam using a superluminescent diode module (Superlum S840-B-I-20) as a seed for a tapered amplifier (Eagleyard 850nm, 500mW). The output of
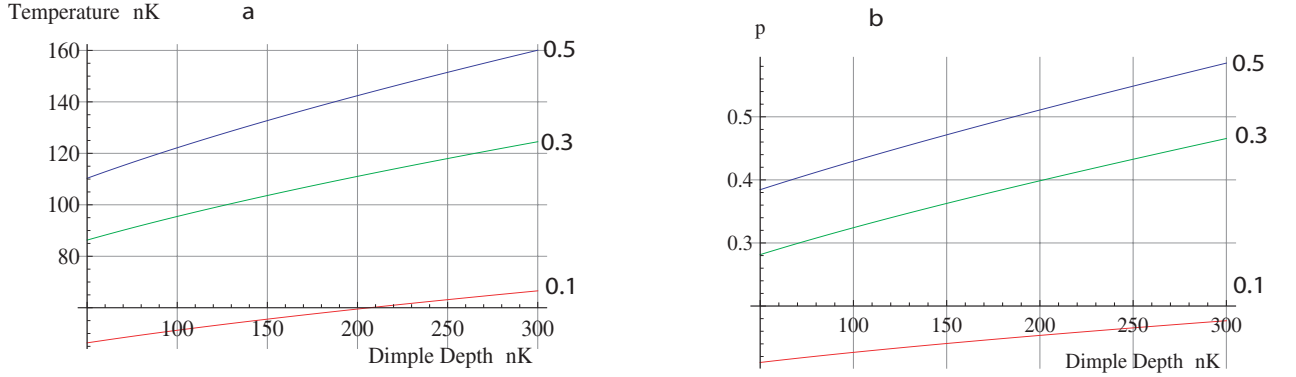
Temperature nK　　a

Figure 4.11: Final temperature of dimple cooling (a) and proportion of atoms retained (b) as a function of the dimple depth for various V_2/V_1 as labeled on the graphs.

the amplifier is shared between two dipole traps, the dimple and the red-dipole that is used in the final stages of the experiment. After filtering out residue 780nm light (Semrock 808 long pass filter), up to 5mW of light can be delivered to the experiment table centered at 824nm with correlation length of 63 μm. We combine the dimple beam path with the fluorescence imaging beam path via a dichroic beamsplitter (Semrock LM01-659-25) as shown in Figure 4.12. To position the beam onto the atoms, we first image the atoms using the Andor camera, then position the reflection of the dimple beam from the superpolished substrate to the same location on the camera. This provides us with only a rough positioning of the beam since the imaging system, focussed on the atom using 780nm light has non negligible focal shift at 840nm. We can also use this to estimate the dimple beam size at the atoms as 7.78 μm $2/e^2$ waist. A more precise alignment is achieved by looking at fluorescence images of atoms in the dimple and ensuring the atoms are in the same position prior to and after loading into the dimple trap.

　　　To load the atoms into the dimple, we ramp up the dimple power to desired values over 200ms as soon as the big lattice reaches full power. The resultant combined potential is shown in Figure 4.13. On completion of the ramp, we reduce the current in all magnetic
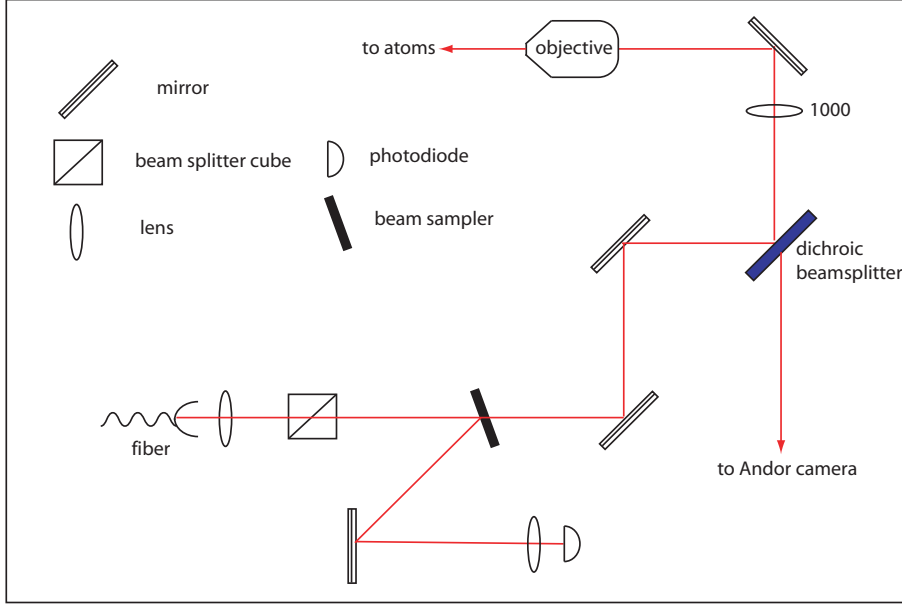
Figure 4.12: Optics setup for dimple beam

field coils in 200 ms before shutting them off completely. At this point, the reservoir atoms not held by the dimple are no longer confined in the transverse direction so will drift out of the region. We typically wait for 100 ms before releasing the atoms from the dimple into a large volume dipole trap in order to ensure that no reservoir atoms remain to the next stage of the sequence. The magnetic fields turn off here prevents us from using arbitrarily low dimple depth since a reasonable large confinement is required to protect the atoms from the violence during the field turn off. This also limits our ability in using the dimple as a tool to reach lower temperature. In order to test whether the dimple satisfies our criteria, we perform fluorescence imaging on the atoms after all the reservoir atoms has been removed. In Figure 4.14, we show the number of atoms retained as a function of the dimple power with the error bar indicating atom number fluctuation calculated over 10 runs. As expected from our previous argument, the atom number is approximately a linear function of the dimple power. Note that the fluctuation in atom number is about 3 % on average (with
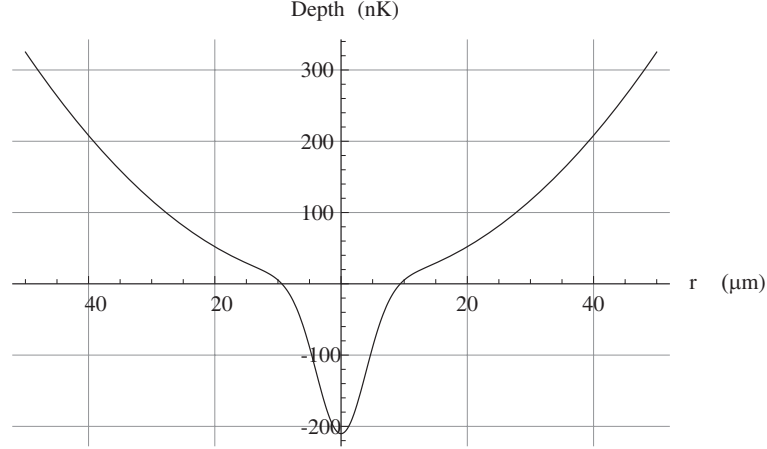
Figure 4.13: Combined potential of the dimple beam plus magnetic field

the exception of 6 % at the lowest dimple power where the atoms probably feel the effect of the field shut off) which is better than our usual 10 % fluctuation in atom number in the cigar trap. We can understand this from equation (4.10). The atom number depends only on the initial density and the geometric properties of the dimple, its width and depth, both are close to being static quantities. Since the peak density in the center of the condensate depends on atom number as $N^{2/5}$, we also have a 60 % reduction in fluctuation. For this low atom number, it is almost impossible to achieve such stability with RF evaporation alone.

4.4   Axial Lattice

While the atoms are in the dimple, we execute an exchange of the vertical confinement by replacing the big lattice with a vertical lattice of greater confinement. The necessity of doing this, stems from the fact that the interaction energy of the atoms in a two dimensional optical lattice is proportional to $\sqrt{\omega_z}$ where ω_z is the frequency in the
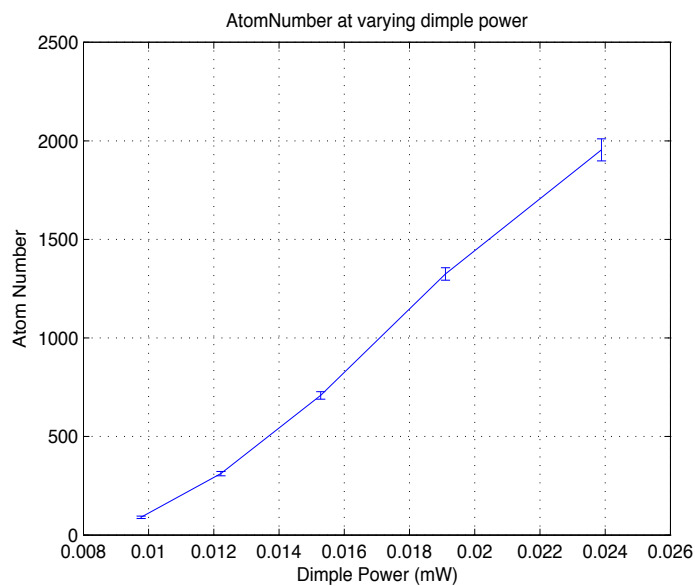
Figure 4.14: Atom number in dimple for varying dimple voltages measured using fluorescence imaging, averaged over 10 repeats. The error bar indicate fluctuation in atom number. A measurement at higher atoms numbers could not be obtained as the cloud size becomes bigger than the effective molasses region.

frozen out vertical direction (see equation (2.13)). It is therefore advantageous for reaching strongly interacting to have as high vertical frequency as possible.

Like the big lattice, the axial lattice is also formed by interference of an incident beam on the flat side of the hemisphere with its reflection from the surface. Here we adjust the angle of incidence to 14.5^o from the surface in order to give a lattice spacing of 1.5 μm. We shape the beam to an aspect ratio of 4 : 1 in order to avoid a highly elliptical cross section at the atoms.

The light source for the axial lattice consist of an amplified spontaneous emission source (Exalos) seeding a tapered amplifier (Eagleyard 765nm, 1.5 W). After filtering out resonant light at 780nm, up to 200 mW of laser power is usable in the experiment with a center wavelength of 756nm and coherence length of 324 μm.

The axial lattice ramps up as soon as all the reservoir atoms not held by the dimple have exited the region. Once reaching full power, the potential due to the big lattice becomes relatively unimportant and can be ramped to 0 rather quickly. After this point, the atoms are held only by optical potentials. Parametric heating measurements here reveal the trap frequencies in the vertical direction reaches 7.1 kHz maximum.

A priori, the location of the atoms in the big lattice need not coincide with the minimum of the axial lattice. The consequence of this being that fluorescence images reveal atoms trapped in the "not in focus planes" of the axial lattice. The motorized mirror in Figure 4.5 allows us to remedy this problem by tuning the big lattice spacing slightly until the big lattice and axial lattice sites coincide. We detect this through a minimum number of background atoms seen in fluorescence images.

4.5   Red dipole

After the atoms are in the axial lattice and the big lattice has been turned off, we execute the very last step of our two dimensional trap formation, by releasing the atoms from the small dimple trap into a large volume red dipole trap. The red dipole is powered by the same light source as the dimple beam. Using the optics setup as shown in Figure 4.15, we center the beam onto the atoms in the same way as for the dimple. Since this beam has a rather large waist of 86 μm, it is not crucial to position the beam waist exactly onto the atoms. We therefore secure all elements in the beam path to fixed positions which should help with beam stability.

As soon as the big lattice has been turned off, we ramp on the red dipole to its final value over 200 ms to a depth of 42 nK. A low trap depth is deliberately chosen here to provide a temperature shield and allow the hot atoms to escape the cloud. The atoms are then released from the dimple to the dipole trap by reducing the dimple power to 0.

We sometimes hold the atoms in this configuration for 6 - 8 seconds to allow the hot atoms produced from the ramp sequences to escape the weak transverse potential. Figure 4.16 shows an example of the fluorescence image of atoms in the all optical trap with frequencies 8 Hz x 7.5 Hz (from red dipole) x 3.4 kHz (from axial lattice) and a 1/e lifetime of 15s. A measurement of the condensate fraction averaged over 10 pictures gives a temperature of 2.6 nK with 1058 atoms. The experimental sequence from the end of RF evaporation in the cigar trap to the end of the all optical surface trap which we use to take the image 4.16 is shown in Figure 4.17.

Although we have used a spatially coherent light from a single mode fiber to make the red dipole beam, it is also possible to do this with the output from a multimode fiber. Since the input light is of short correlation length (temporally incoherent), when
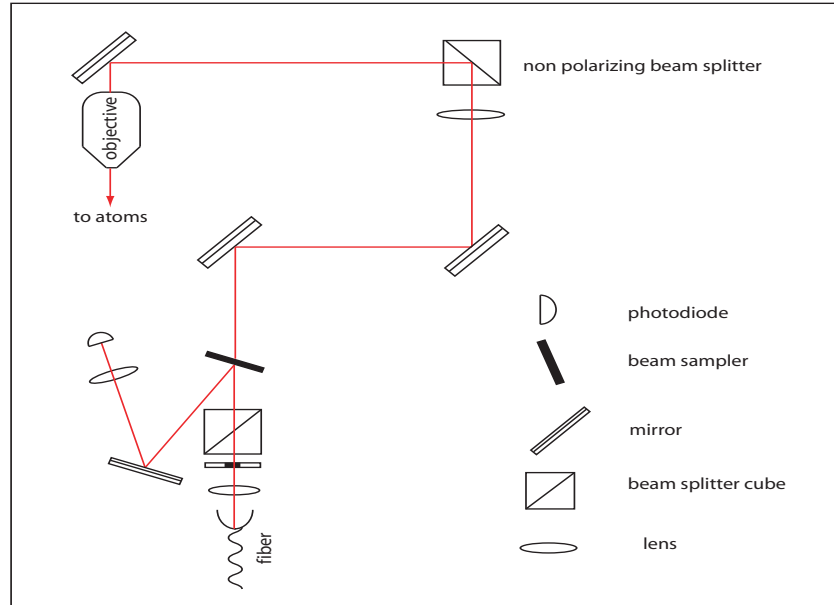
Figure 4.15: Optics setup for the red dipole beam. The beam is combined with the imaging path via a non polarizing beamsplitter
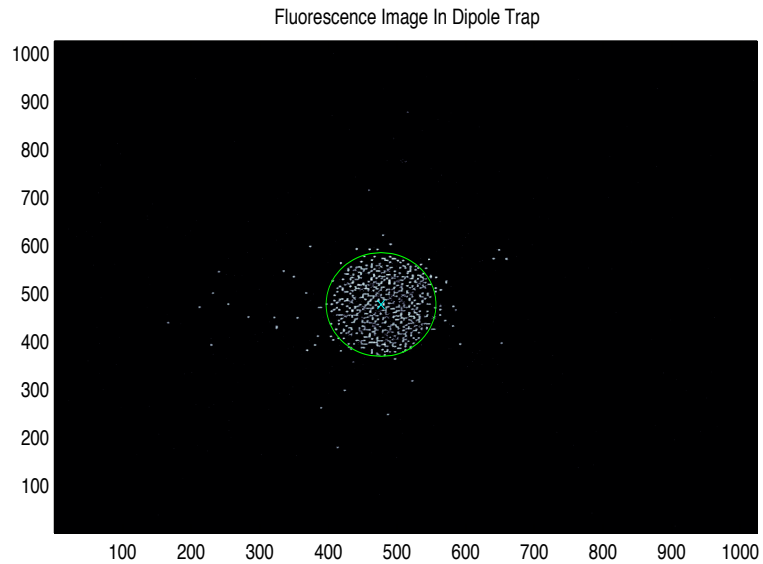

Figure 4.16: Fluorescence image of atoms in the optical trap. The solid ellipse shows the boundary of the Thomas Fermi profile from which the condensate fraction was determined.
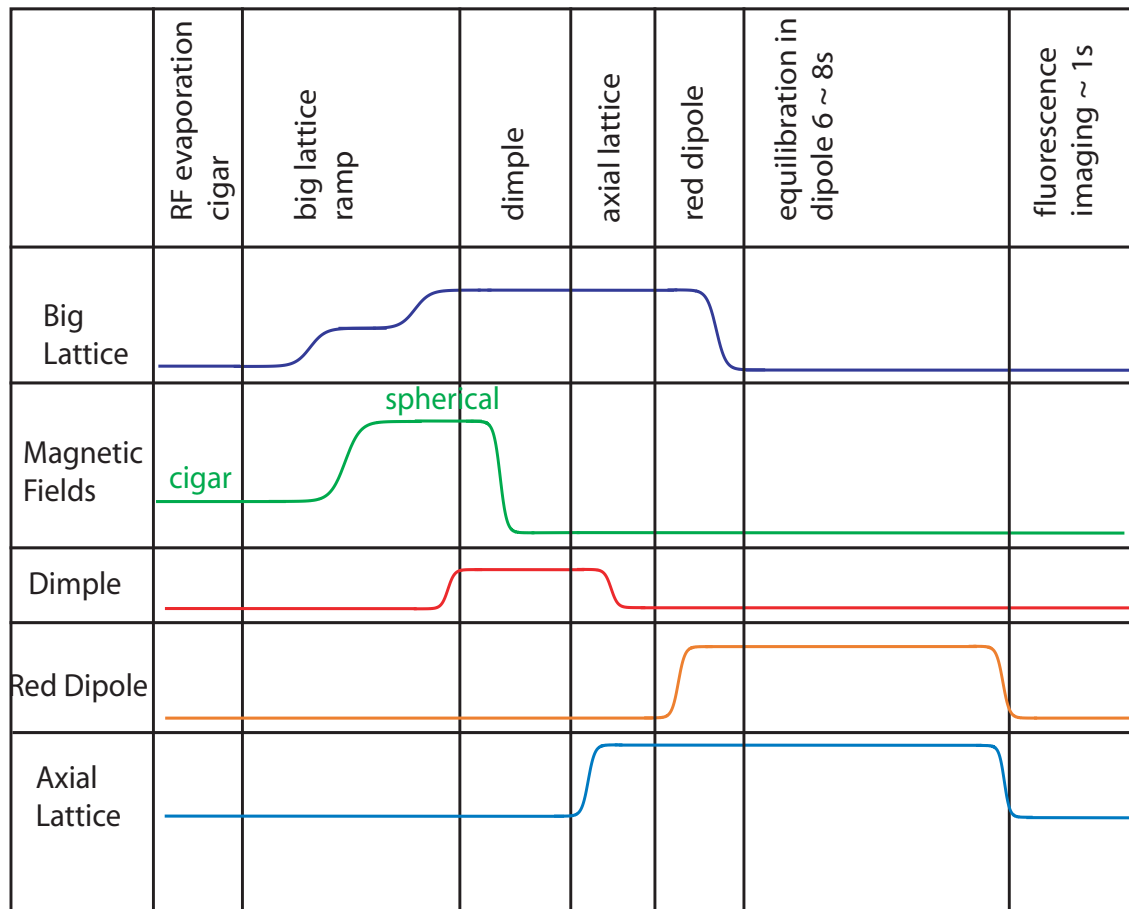
Figure 4.17: Ramp sequences from end of evaporation to all optical surface trap.

the path difference of the various fiber modes exceeds the coherence length, the output is free of speckle patterns. The use of such beam has two advantages over spatially coherent light. One, the potential is less susceptible to local perturbations in the beam path since such disturbances are unable to produce long range modulations by interference with the remainder of the beam. This is particularly helpful when the size of the beam needs to be very large (such as the beams that forms the two dimensional optical lattice), as spatially coherent beams in such instances often suffer from inhomogeneous profile due to dust or scratches on optical elements in the beam path. Secondly, beam profile from multimode fibers can differ from Gaussian depending on the distribution of the fiber modes, This could be changed by the in-coupling condition into the fiber or by applying force on a segment of the fiber (this changes the local cross section and allow the different fiber modes to mix). We can use this property to generate different confinement geometry for the atoms.

Working with spatially incoherent light can be rather troublesome however, as most beams diverges very fast unless it is large already. Because of this, distances between consecutive optical elements must be kept short and large sized optics must be used to prevent unwanted beam clipping. Note that unlike a spatially coherent beam from a single mode fiber, any unintended apertures here can change the beam profile and power significantly since there are a significant number of spatial modes with extent far from the beam center.

To test the feasibility of incoherent light, we take the single mode fiber output previously used for the red dipole and butt couple it to a multimode fiber. The multimode fiber used here is a 105 μm core diameter, 100 m long step index fiber. We purchase the fiber without a jacket so as to allow mode scrambling by applying pressure to the fiber. The fiber tip is then imaged by a succession of four lenses onto the atoms.

Again we examine the beam profile at the atoms by looking at the reflection from
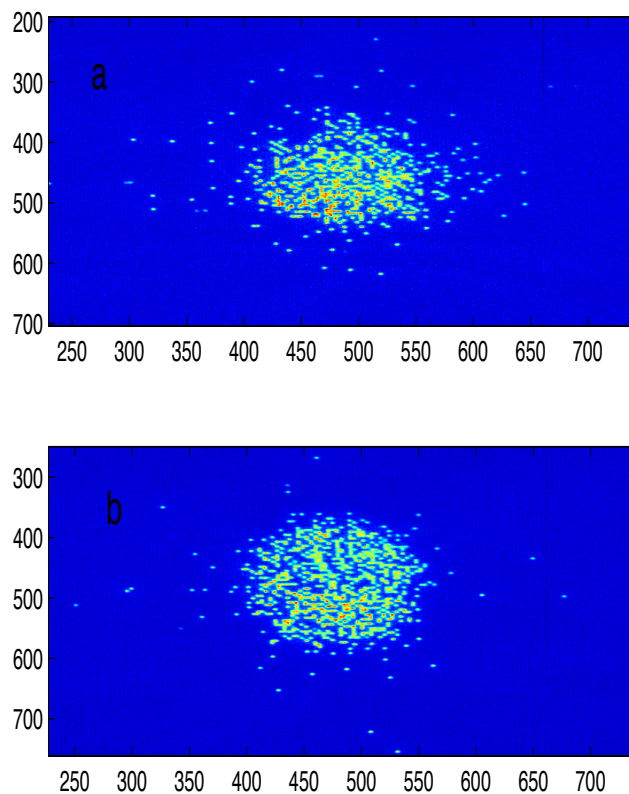
Figure 4.18: Atoms in dipole trap made with a. spatially incoherent light and b. spatially coherent light.

the superpolished substrate. In Figure 4.19, the beam shows a rather large gaussian profile with some small corrugations that arose from residue spatial coherent of the beam and its large size. Significant care was taken here to ensure that beam clipping is kept to a minimum. The fluorescence images of the atoms (see Figure 4.18) in this dipole trap and one made with a spatially coherent light exhibit no major differences.

By applying pressure to the fiber and aperturing the beam afterwards, it is also possible to obtain a more flat topped profile as shown in Figure 4.19. The power loss in this process is quite significant therefore we did not have enough power to make a dipole
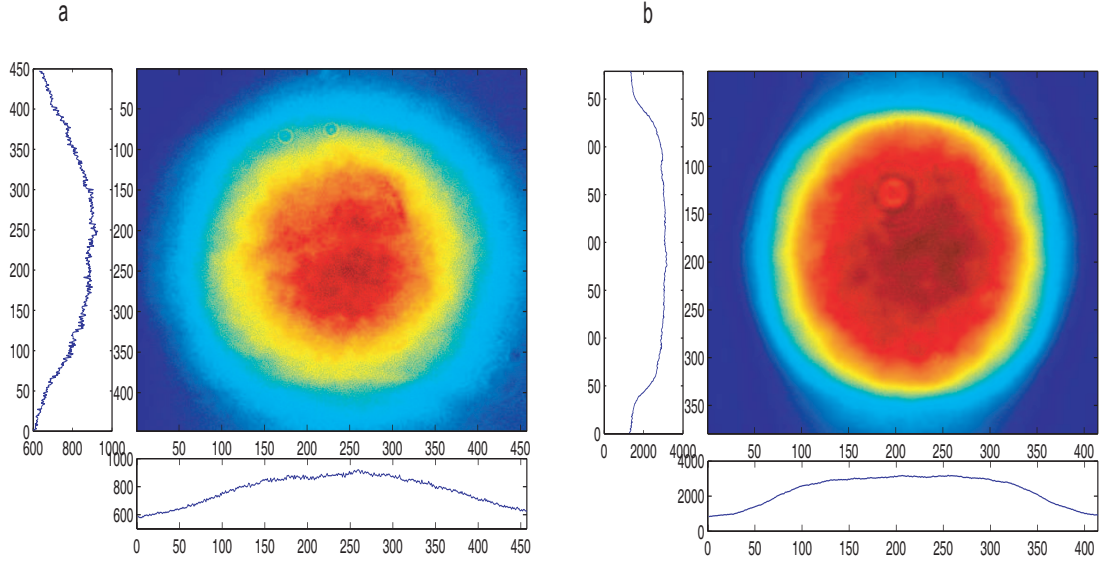
Figure 4.19: a. Reflection from superpolished surface of spatially incoherent dipole beam. b. After mode scrambling, the beam profile become flat topped.

trap using this geometry.

As a check to see if this configuration satisfied our original motivation, we have verified that the atoms in this 2D trap expanded freely within the axial lattice and no atoms were pinned due to adsorbed atoms on the glass surface. [2] After almost one year in operation, we have yet to detect any evidence of this trap suffering from surface effects.

The end of the red dipole ramp is also the starting time for our experiments in two dimensional optical lattice. The following chapters are devoted to the details of our lattice beam set up and the experiments we are able to realise.

---

[2]The expansion within the axial lattice is still anisotropic due to the corrugations in the profile of the axial lattice beam which is unrelated to the problem of adsorbed atoms on the glass surface

Chapter 5

Theory of Atoms In Optical Lattice

In this chapter, we introduce the theoretical concepts related to neutral bosons in optical lattice potentials and how they can be used for simulating the Bose Hubbard Hamiltonian. Previously considered a toy model in condensed matter theory, the Bose Hubbard Hamiltonian has been studied extensively by cold atom experimentalists in recent years. This has yielded several interesting insights into the nature of its quantum phase transition.

5.1 Single Particle In Lattice Potential

We start by considering the dynamics of one neutral particle subjected to the periodic potential of a blue detuned one dimensional lattice in the x direction. The single particle Hamiltonian applicable to us is

$$\mathcal{H} = -\frac{\hbar^2}{2m}\nabla^2 + \frac{V_L(y,z)}{2}\left(1 - \cos(2kx)\right) \tag{5.1}$$

The second term of (5.1) denotes the periodic potential created by the interference of the two light beams that forms the lattice. The lattice wave vector k is related to the lattice

spacing a_L via $k = \pi/a_L$ and defines the characteristic energy scale of the lattice, the recoil energy $E_R = \frac{\hbar^2 k^2}{2m}$ to which we measure all other energy scales with respect to. Here we assume counter propagating beams parallel to the x axis, so the transverse profile of the beam occurs in the (y,z) plane. In general, due to the Gaussian intensity profile of the beam, there is a slow variation in the lattice depth as one moves away from the center of the beam. However for distances close to the center of the Gauss beam, we can treat the lattice depth as approximately constant, given by its value at the beam center and account for the effect of the Gaussian profile by the addition of a slowly varying parabolic potential.

Let us first consider the solution of (5.1) with a spatially constant lattice depth. According to Bloch's theorem [11], the eigenstates of (5.1) with a constant V_L can be chosen to be of the form

$$\psi_{nq}(x) = e^{iqx}\, u_{nq}(x) \tag{5.2}$$

where the function $u_{nq}(x)$ has the same periodicity as the lattice. The indices n,q of the Bloch wavefunction (5.2) denotes the band index and Bloch wavevector respectively where the wavevector is restricted to within the first Brillouin zone $q \in [-k, k)$ only. The eigenvalues of (5.2), ϵ_{nq} shown in Figure 5.1 gives the energy bands of the atoms in the lattice and characterise the energy of single particle dynamics in the potential.

The Bloch wavefunction provides an adequate description of the atoms in the lattice at low lattice depths when the atomic wavefunction is spread over many lattice sites. Furthermore, we carry out our experiment by loading a stationary condensate into a stationary lattice, thereby populating primarily the lowest n = 0 energy band and quasimomentum q = 0.

To account for the Guassian profile of the lattice beams, we first observe that for a red detuned lattice where the lattice sites corresponds to location of maximal light intensity, the primary effect of the beam profile is to provide a spatially varying energy offset (stark
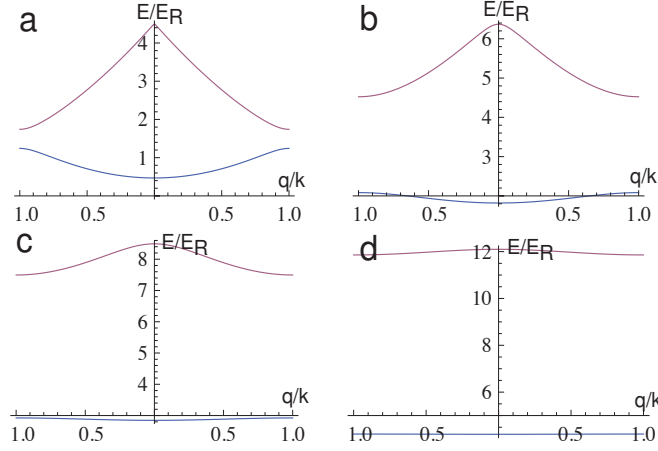
Figure 5.1: Energy of the first two bloch bands in units of recoil energy ($E_R = 1.48$ kHz) for one dimension lattice of spacing 620nm. Horizontal axis is quasi-momentum in units of lattice reciprocal wavevector and vertical axis shows band energy in units of E_R. The lattice depths are a) 1 E_R, b) 5 E_R, c) 10 E_R and d) $20E_R$. Notice that the gap between the bands at $q = 0$ is bounded below by about 4 E_R, which is not true for q=k at the edge of the Brillouin zone. The band width becomes increasing flat as the lattice depth increases signifying the much reduced tunnel coupling between the lattice sites.

shift) to each lattice site owing to the different local light intensity. The secondary effect of the intensity profile is to modify the local lattice depth, causing the atomic wavefunction and hence the band energy to change in space. Although this contribution is also present for a red detuned lattice, its effect is considerably less than the variation in local AC stark shift. For a blue detuned lattice however, the former effect is almost absent since the lattice sites correspond to intensity minimum. Therefore, the consequence of the beam profile is to cause the atoms to experience reduced lattice depth further away from the center of the beam, hence the eigen energy of the atomic wavefunction will vary in space. To calculate this effect we note that the intensity variation occurs on the scale of a beam waist (about 145 μm for us) which is much greater than the lattice spacing of 620 nm. Thus over the distance scale of a few lattice sites, the lattice depth can be considered as approximately constant, we can therefore perform a local density approximation : that is, for low lattice
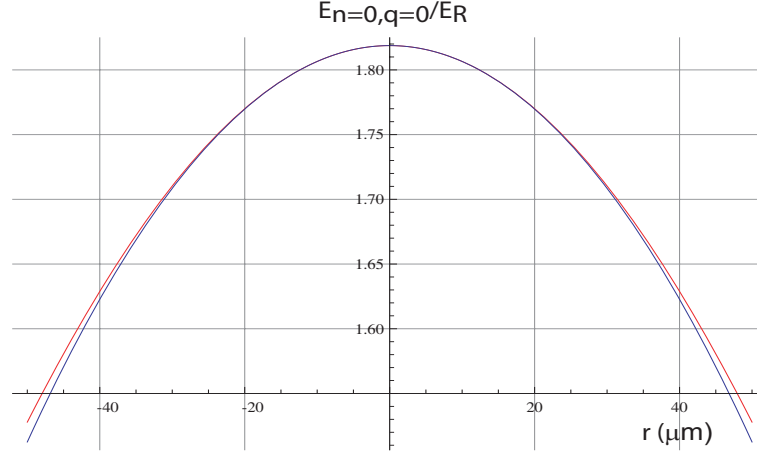
Figure 5.2: Energy of condensate in the n $= 0$, q $=0$ state across the lattice beam with Gaussian waist of 145 μm, calculated in the local density approximation (red) and the parabolic approximation using the curvature at the beam center (blue) as described in the text.

depths (in the superfluid regime) the atoms are in the Bloch state $n = 0 = q$ whose energy at any point in space is simply the band energy calculated for a homogeneous system at the locally prevailing lattice depth. The resultant spatial variation is shown in Figure 5.2 from which we can extract the parabolic approximation valid near the beam center. This allows us to write an approximation to the full Hamiltonian (5.1) as

$$\mathcal{H} = -\frac{\hbar^2}{2m}\nabla^2 + \frac{V_L}{2}\left(1 - \cos(2kx)\right) - \frac{1}{2}m(\omega_y^2\, y^2 + \omega_z^2\, z^2) \tag{5.3}$$

where V_L is the lattice depth at the beam center and the overall deconfinement from the lattice beams is given by

$$m\omega_y^2 = \left|\frac{\partial^2}{\partial y^2}\epsilon_{n=0,q=0}\left(V_L e^{-\frac{2y^2}{w^2}}\right)\right| \tag{5.4}$$

where w is the lattice beam waist.

When the lattice is sufficiently deep to localize the atoms, the Bloch function is no longer a good description of the atom's wavefunction. Instead, we switch to a different basis wavefunction, describing atoms partially localized to a single lattice site. Such a basis
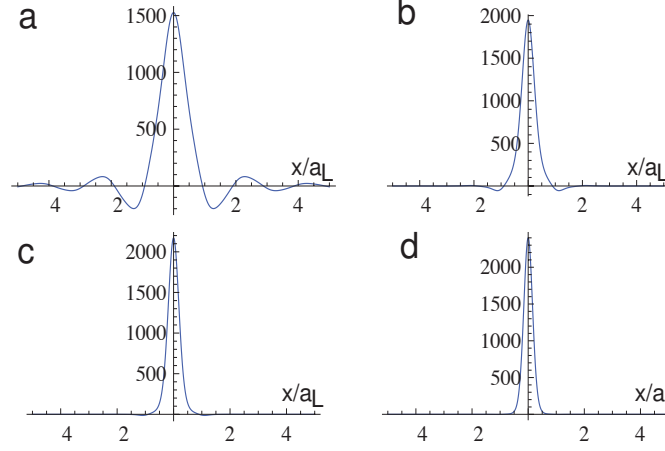
Figure 5.3: Wannier function at various lattice depth. Horizontal axis shows distance in units of lattice spacing (620nm). The lattice depths are a) 1 E_R, b) 5 E_R, c) 10 E_R and d) 20 E_R. The recoil energy is $E_R = 1.48$ kHz

function (called Wannnier function) can be constructed from the Bloch states as

$$w_0(x - R) = \frac{1}{\sqrt{\mathcal{N}}} \sum_q e^{-iqR} \psi_{n=0,q}(x)$$

where $\mathcal{N}$ is a normalisation constant and the sum is over all quasimomentums in the first Brillouin zone. Note that the Wannier function shows increase localization at greater lattice depth but nevertheless has small penetration into adjacent lattice sites.

With this new set of basis, valid for deep lattices we can return to examine the consequence of a spatially varying lattice intensity for deep lattices. The local density approximation still applies, except we must now calculate the energy not in the $n = q = 0$ Bloch state but with respect to the Wannier state. Figure 5.4 shows the resultant energy variation across the lattice beam together with the parabolic approximation calculated using the *Bloch band energy*, equation (5.4). Although not exact, we see that the curvature from the band structure calculation continues to be good at deeper lattice depths. We may have expected this result following the observation that the mean energy in the Wannier state is
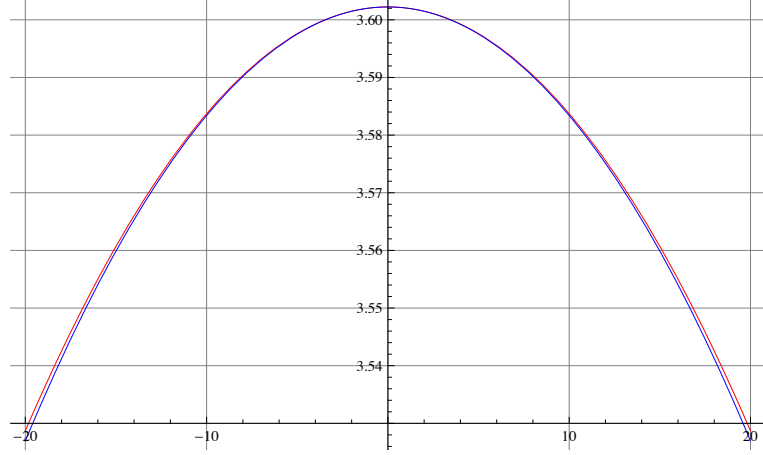
Figure 5.4: Energy expectation of the Wannier state with a Gaussian intensity profile (red) with center lattice depth of $15E_R$. The blue curve shows the parabolic approximation using the trap frequency calculate from equation (5.4) with the same lattice depth.

simply the average Bloch energy within the lowest band.

$$\langle w_0 | H(V_L) | w_0 \rangle = \frac{1}{N_{lat}} \sum_q \epsilon_{n=0,q}(V_L)$$

As the lattice depth increases, the band becomes flatter so that asymptotically we have

$$\lim_{V_L \to \infty} \frac{1}{N_{lat}} \sum_q \epsilon_{n=0,q}(V_L) = \epsilon_{n=0,q=0}(V_L)$$

hence we recover the same expression as in (5.4). We fit equation (5.4) to a sixth order polynomial plus a square root in V_L/E_R, this function is then used during the experiment for adjusting the overall external confinement during the lattice ramp up.

5.2 Two Dimensional Optical Lattice

For the simple cubic lattice in two dimensions, which we use in our experiment, the lattice potential is

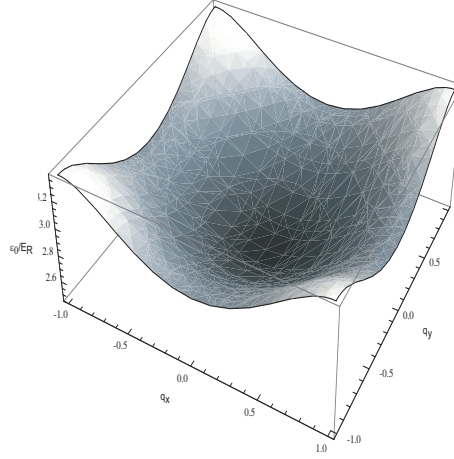$$U_{Lat}(x,y) = \frac{V_L^x}{2}(1 - \cos(2kx)) + \frac{V_L^y}{2}(1 - \cos(2ky))$$

Figure 5.5: Lowest energy band of two dimensional simple cubic lattice within the first Brillouin zone at lattice depth of 3 E_R.

since the two orthogonal axes are decoupled, the dynamics therefore reduces to two independent one dimensional lattices. The first Brillouin zone of the lattice is a square in quasimomentum space and Figure 5.5 shows the energy of the lowest band in the two dimensional first Brillouin zone which is simply the sum of the Bloch energies in the two axes

$$\epsilon_{n,(q_x,q_y)} = \epsilon_{n,qx} + \epsilon_{n,qy}$$

The two dimensional Bloch function and Wannier functions are simply products of the corresponding functions in each directions

$$w_0(x,y) = w_0(x)w_0(y) \qquad \psi_{n,q_x,q_y}(x,y) = \psi_{n,q_x}(x)\psi_{n,q_y}(y)$$

5.3   Bose Hubbard Model

Much of the driving force behind the recent surge of research into optical lattices stem from the pioneering work of D. Jaksch *et. al.* [12] when they showed that neutral bosons in optical lattice realises the Bose Hubbard Hamiltonian. In this section we show

how this is possible and give estimation of the Bose Hubbard parameters realisable with
our system.

Let us first examine how the cold atoms in optical lattice system could be trans-
formed into the Bose Hubbard Hamiltonian. In second quantisation, the Hamiltonian for a
weakly interacting bose gas in a two dimensional lattice is

$$\mathcal{H} = \int \hat{\Psi}^\dagger(\mathbf{r}) \left[-\frac{\hbar^2}{2m}\nabla^2 + U_{Lat}(\mathbf{r}) + \frac{1}{2}m\omega^2 r^2 \right] \hat{\Psi}(\mathbf{r})\, d^3\mathbf{r} + \frac{1}{2}\frac{4\pi\hbar^2 a}{m}\sqrt{\frac{m\omega_z}{2\pi\hbar}} \int \hat{\Psi}^\dagger(x)\hat{\Psi}^\dagger(x)\hat{\Psi}(x)\hat{\Psi}(x)\, d^3\mathbf{r}$$

$$(5.5)$$

where the parabolic confinement on top of the lattice potential in our experiment arises
from the combined effect of an auxiliary red detuned dipole trap and the blue detuned
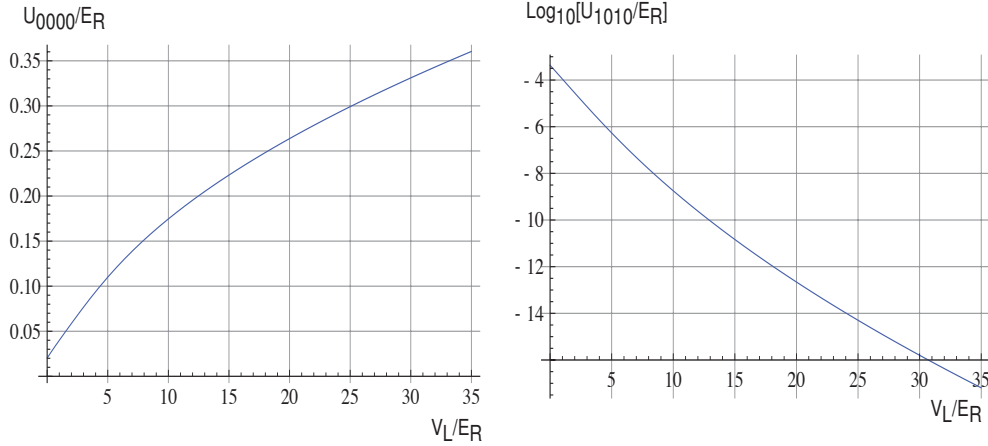lattice beams.

Figure 5.6: Comparison of onsite (left) and nearest neighbour (right) interaction energy for
various lattice depth showing that we are justified in ignoring the next nearest neighbour
contribution. Parameters calculated for a two dimensional simple cubic lattice with 7.1 kHz
trap frequency in the frozen out direction.

Within the tight binding approximation and occupation of only the lowest band,
we can expand the field operator as a sum over all the lattice sites using the Wannier
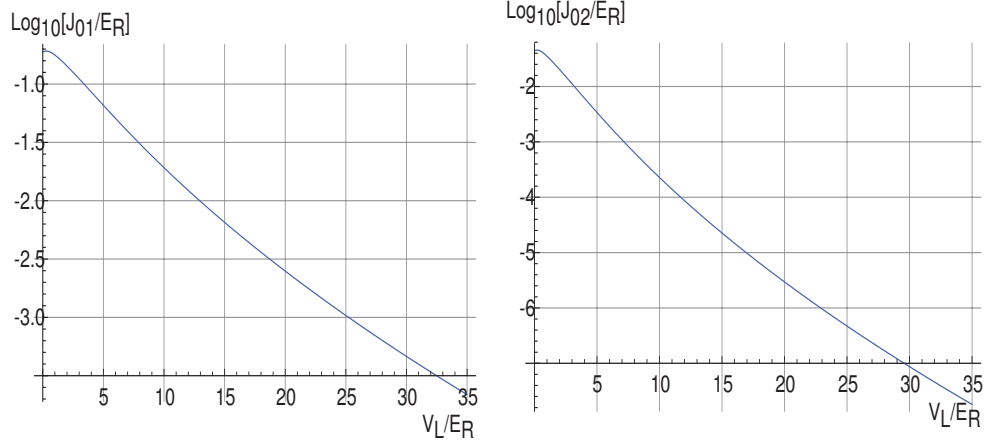
Figure 5.7: Comparison of nearest neighbour tuneling and ndext nearest neighbour tunelling for various lattice depth. The nearest neighbour tuneling dominates. Parameters calculated for a simple cubic lattice with 7.1 kHz trap frequency in the frozen out direction

functions as the basis

$$\hat{\Psi}(x) = \sum_i w_0(\mathbf{r} - \mathbf{r}_i) \, \hat{b}_i \tag{5.6}$$

where $\hat{b}_i$ is the annihilation operator for the lattice site i and $w_0(\mathbf{r} - \mathbf{r}_i)$ is the Wannier function characterising the wavefunction of an atom localised at lattice site i. Substituting (5.6) into (5.5) we obtain the many body Hamiltonian as

$$\hat{H} = -\sum_{i,j} J_{ij} \, \hat{b}_i^\dagger \, \hat{b}_j + \frac{1}{2} \sum_{i,j,k,l} U_{ijkl} \, \hat{b}_i^\dagger \, \hat{b}_j^\dagger \, \hat{b}_k \, \hat{b}_l + \sum_i \epsilon_i \, \hat{b}_i^\dagger \, \hat{b}_i - \mu \sum_i \hat{b}_i^\dagger \, \hat{b}_i \tag{5.7}$$

the chemical potential μ occurs in the grand canonical ensemble to ensure normalisation to the correct total atom number, and ϵ_i is the energy offset at lattice site i due to an external parabolic confinement.

The two Bose Hubbard parameters can be calculated from the Wannier function as

$$J_{ij} = -\int w_0^*(\mathbf{r} - \mathbf{r}_i) \left(-\frac{\hbar^2 \nabla^2}{2m} + U_{Lat}(\mathbf{r}) \right) w_0(\mathbf{r} - \mathbf{r}_j) d^3\mathbf{r} \tag{5.8}$$

which characterise the kinetic energy term inducing hopping from lattice sites i to lattice site j. And the interaction term that characterise the repulsion between atoms close to each

other

$$U_{ijkl} = \frac{4\pi\hbar^2 a}{m}\sqrt{\frac{m\omega_z}{2\pi\hbar}}\int w_0^*(\mathbf{r}-\mathbf{r}_i)\,w_0^*(\mathbf{r}-\mathbf{r}_j)\,w_0(\mathbf{r}-\mathbf{r}_k)\,w_0(\mathbf{r}-\mathbf{r}_l)\,d^3\mathbf{r} \qquad (5.9)$$

In accordance with the tight binding approximation, we may keep only the dominant nearest neighbour hopping terms in (5.8) corresponding to i and j being nearest neighbours, and the onsite interaction term in (5.9) corresponding to $i = j = k = l$. Figures 5.6 and 5.7 shows that our approximation is well justified since the next order terms are indeed much smaller. This then leads to a simplified Bose Hubbard Hamiltonian [13]

$$\hat{H}_{BH} = -J\sum_{\langle i,j \rangle} \hat{b}_i^\dagger \hat{b}_j + \frac{U}{2}\sum_i \hat{b}_i^\dagger \hat{b}_i^\dagger \hat{b}_i \hat{b}_i + \sum_i \epsilon_i\, \hat{b}_i^\dagger \hat{b}_i - \mu\sum_i \hat{b}_i^\dagger \hat{b}_i \qquad (5.10)$$

with

$$J \;=\; J_{10} = -\int w_0^*(\mathbf{r}-\mathbf{r}_i)\left(-\frac{\hbar^2\nabla^2}{2m} + U_{Lat}(\mathbf{r})\right)w_0(\mathbf{r}-\mathbf{r}_j)\,d^3\mathbf{r}$$

$$U \;=\; U_{0000} = \frac{4\pi\hbar^2 a}{m}\sqrt{\frac{m\omega_z}{2\pi\hbar}}\int |\omega_0(\mathbf{r})|^4\,d^3\mathbf{r} \qquad (5.11)$$

The ground state of the many body Hamiltonian at a fixed μ is determined by the relative magnitude of U and J. Their ratio is shown in Figure 5.8 together with the value that marks the quantum phase transition into the $n = 1$ mott insulator state.
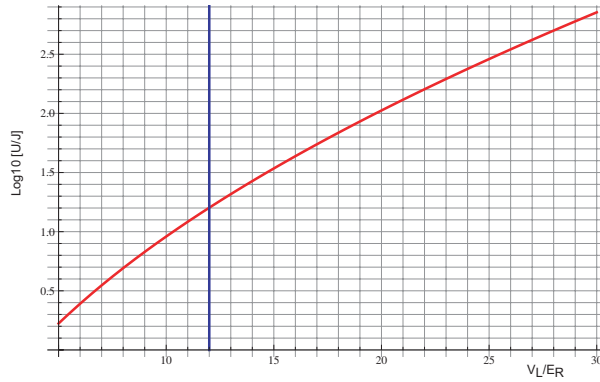

Figure 5.8: Plot of U/J for various lattice depth (red). The blue line marks the lattice depth for transition from superfluid to n = 1 mott insulator in a homogeneous system.

It is useful here to obtain some approximation expressions for U and J that captures their qualitative dependent on the lattice depth within the tight binding approximation. The probability for an atom localized at site 0 to tunnel to the adjacent lattice site a distance a_L away could be calculated using the WKB approximation for transmission through a deep barrier

$$J = e^{-2\sqrt{\frac{2m}{\hbar^2}} \int_0^{a_L} \sqrt{U_{Lat}(x')-E} dx'} \approx e^{-2\sqrt{\frac{2m}{\hbar^2}} \int_0^{a_L} V_L \sin(\frac{\pi x'}{a_L}) dx'} = e^{-4\sqrt{\frac{V_L}{E_R}}}$$

a more precise calculation as shown in [25], gives that

$$\frac{J}{E_R} \approx \sqrt{\frac{8}{\pi}} \left(\frac{V_L}{E_R}\right)^{3/4} e^{-2\sqrt{\frac{V_L}{E_R}}}$$

The approximate behaviour of U can be captured by noting that the Wannier function within a lattice site is well approximated by the lowest energy harmonic oscillator state within each well. Substituting this for the Wannier function in (5.9) gives

$$\frac{U}{E_R} \approx 4a\sqrt{\frac{m\omega_z}{2\pi\hbar}} \sqrt{\frac{V_L}{E_R}} \tag{5.12}$$

so we see that for deep lattices, the tunneling decreases exponentially with the lattice depth while the interaction increases only polynomially.

5.4   Superfluid to Mott Insulator Transition

It was shown in [13] that the Bose Hubbard Hamiltonian undergoes a zero temperature phase transition when the ratio of U/J exceeds a critical value [1]. We can see this might be the case heuristically, by considering the two extremal cases for a homogeneous system ($\epsilon_i = 0$ in equation (5.9)). In the limit of $J \ll U$, the eigenstates of (5.9) tends to integer number of atoms $n_0 = [\mu/U]$ on each lattice site with no phase correlations between

---

[1]This transition also occurs at finite temperatures up to 0.2 U [29]

the lattice sites (since there is very little hopping between them). As U is the dominant energy scale in this regime, there are expensive energy costs to having more than n_0 atoms per site which discourages fluctuations in site occupation. This state is usually referred to as the Mott insulator state and is characterised by the features of reduced atom number fluctuation on lattice sites, absence of phase correlation between lattice site, and zero compressibility. In the opposite extreme, when $U \ll J$, tunneling is prevalent throughout the entire lattice and every site maintains a fixed phase relation relative to the other lattice sites. This state is termed the superfluid and is characterised by the existence of long range phase coherence across the lattice.

The phase diagram of (5.9) for a homogeneous system can be calculated in the mean field approximation [14]. The result shows lobe like regions (Figure 5.9) in phase space where the ground state of the system is a Mott insulator with integer number of atoms per lattice sites. For a square lattice in two dimensions, the mean field prediction gives transition from superfluid to Mott insulator of one atom per site as occurring first at $U/J = 23.8$ which is different from the actual transition at $U/J = 16$ confirmed by recent experiments [17, 16, 15] and by Monte Carlo simulations [21].

5.5   Inhomogeneous System - Mott Insulator Shells

In the presence of an external harmonic confinement, one can have a co-existence of superfluid and mott insulator states. We consider the experimentally relevant case when the external confinement is slowly varying such that the local density approximation is applicable.

In the superfluid phase, $zJ \ll U$, we expect the wavefunction of each atom to be delocalized over the whole cloud (just as in the case of a Bose Einstein Condensate)
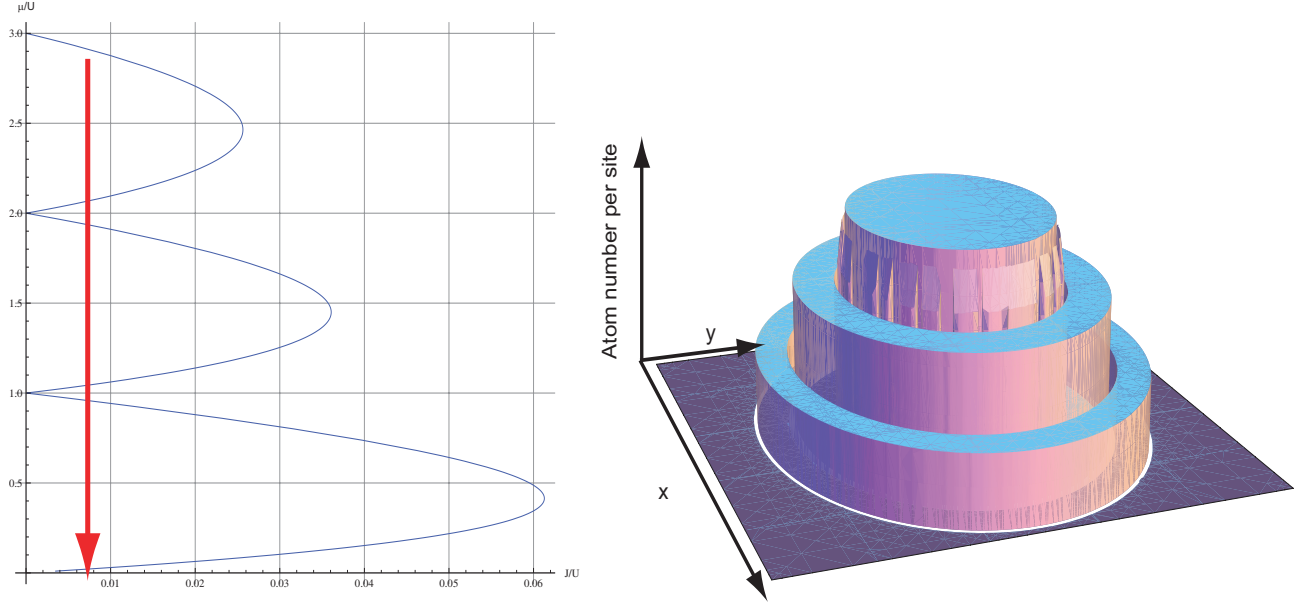
Figure 5.9: Phase diagram of the Bose Hubbard hamiltonian for a two dimensional homogeneous system simple cubic lattice calculated using mean field. The lobe like regions is where the system ground state is a mott insulator. Here we attempt to account for the inadequacy of the mean field theory by adjusting the number of nearest neighbours parameter to match the superfluid to n = 1 Mott insulator transition point to the value determined from experiments. The resultant phase diagram match closely with Monte Carlo simulation in location of the lobe tips in parameter space but is unable to capture the asymmetry between the upper and lower branch of the lobes. In an inhomogeneous system, as in the presence of an external harmonic trap the local chemical potential sweep through various values as shown by the vertical arrow in the phase diagram which leads to the occurrence of mott insulator shells.

so that the overall density profile should resemble that of a harmonically confined BEC with modification to account for the increase in interaction strength due to the presence of the lattice. We apply the mean field approach here and replace the operators in (5.10) with complex numbers $\hat{b}_i \to \psi_i$ such that the occupation of site i is given by $n_i = |\psi_i|^2$. Substituting for $\epsilon_i = 1/2 m \omega_{tot}^2 r_i^2$ as for a harmonic potential, we obtain the following equation for the energy of the system

$$\langle \hat{H}_{BH} \rangle = -J \sum_{<i,j>} \psi_i^* \psi_j + \frac{U}{2} \sum_i |\psi_i|^4 + \frac{1}{2} m \omega_{tot}^2 \sum_i r_i^2 |\psi_i|^2 + \mu \sum_i |\psi_i|^2 \qquad (5.13)$$

in the limit of a large cloud, we can apply the Thomas Fermi approximation and neglect the kinetic energy term proportional to J. After minimizing with respect to ψ_i we obtain its equation of motion

$$U|\psi_i|^2\psi_i + \frac{1}{2}m\omega_{tot}r_i^2\psi_i = \mu\psi_i$$

so that the density profile is

$$n(\mathbf{r}_i) = \max\left[\frac{\mu - \frac{1}{2}m\omega_{tot}^2 r_i^2}{U}, 0\right] = n_{peak}\max\left[1 - \frac{r_i^2}{R^2}, 0\right] \tag{5.14}$$

where the Thomas Fermi radii is

$$R^2 = \sqrt{\frac{4NUa_L^2}{\pi m\omega_{tot}^2}} \tag{5.15}$$

for a total of N atoms in the cloud.

In the Mott insulator regime, the situation is more complicated. Since the local chemical potential ($\mu_i = \mu - \epsilon_i$) sweeps through various values in the phase diagram as shown in Figure 5.9. This leads to the presence of a Mott insulator shell structures. We can obtain some estimates for the size of the shell structure in the following ways : for J = 0, the transition from $n \to n - 1$ Mott insulator state occurs at the radius R_n such that $\mu - 1/2m\omega_{tot}^2 R_n^2 = (n-1)U$. The constant chemical potential μ at the center of the trap is chosen in such a way that the total atom number is correct. For a circularly symmetric geometry, each successive Mott insulator region contributes an extra 1 particle per lattice site so that

$$N = \sum_{n=1}^{[\frac{\mu}{U}]} \frac{\pi R_n^2}{a_L^2} = \frac{2\pi U}{ma_L^2\omega_{tot}^2}\left(\frac{\mu}{U}\left[\frac{\mu}{U}\right] + \frac{1}{2}\left[\frac{\mu}{U}\right]\left(1 - \left[\frac{\mu}{U}\right]\right)\right) \tag{5.16}$$

For a given set of experimental parameters, we solve equation (5.16) for μ graphically.

At finite but small tunneling, we assume that the value of μ calculated for the zero tunneling case persists and use the mean field phase diagram of Figure 5.9 to solve for the local chemical potentials at the upper and lower boundary of each Mott lobe. As an improvement over just mean field calculation, we adjust the number of nearest neighbour
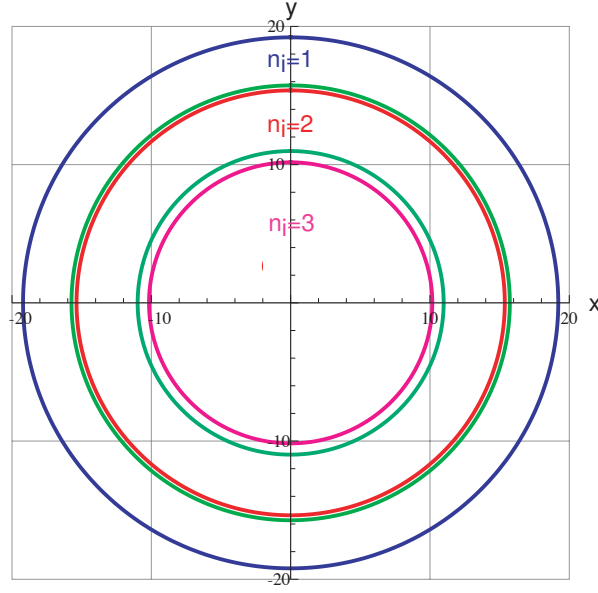
Figure 5.10: Theoretical region of Mott insulator shells calculated for initial confinement $\omega_{tot} = 17Hz$ with final lattice depth of 22 E_R and 1800 atoms in total

parameter in the mean field model such that the tip of the lobes matches the lobe location from the more precise quantum Monte Carlo calculations, resulting in the effective number of nearest neighbours $z = 2.9$. Although this fails to capture the asymmetry between the upper and lower branches of each Mott lobe, the discrepancy appears small at low tunneling values. An example of the calculated Mott insulator regions is shown in Figure 5.10, calculated for realisable parameters in our experiment. Notice that the size of the superfluid region in between the Mott shells have a spatial extent on order of a few lattice spacing, which preclude them from direct observation except for experiments using high resolution imaging systems. The presence of Mott insulator shells has been verified in previous experiments using spin changing collisions [18] and atom number induced shift to atomic clock resonance frequency [19].

Chapter 6

Experiments With Optical Lattice

In this chapter, we describe our setup for generating the optical lattice potential which is unlike the method utilised by most other groups. Our technique affords us many possibilities for extending the current repertoire of optical lattice experiments, such as the study of dynamical and arbitrary lattice potentials.

We then describe how the atoms are loaded into the lattice in order to maintain the system in the ground state of the many body Hamiltonian. Our procedure allows us to see signatures of superfluid to mott insulator phase transition in the time of flight images of atoms released from the optical lattice. Finally we briefly outline some in-situ observation of mott insulator shells in our experiment which is only possible through the use of high resolution imaging system.

6.1 Optical Lattice Generation

Most optical lattice experiments to date generate the lattice potential by interfering independent pairs of counter-propagating beams. Because of the proximity of our atoms location to the hemispherical surface, generating the lattice pattern this way is rather

cumbersome. However the high numerical aperture microscope offers a convenient solution to overcome this problem : it is possible to image the lattice pattern from a transmission hologram or mask onto the atoms. We achieve this using the same set of optics as was used to generate the lattice that pins the atoms during imaging (see section 3.2).

The possibility of imaging the light potential is not new [58, 59, 60]. This method of lattice generation affords us several flexibilities not possible with interfering separate generated beams. Because the light pattern is imaged onto the atoms, one simply has to manufacture a new mask pattern in order to generate different potential landscapes which need not even be periodic [1]. Secondly because the lattice pattern is imaged onto the atoms, the lattice structure is independent of the wavelength or light used to illuminate the hologram. This allows us to use the same optics setup to generate lattice potentials near resonance and far detuned wavelength which is the crucial ingredient that allows our imaging procedure to work. Thirdly, we can easily generate time varying potentials by using computer controlled hologram patterns such as a spatial light modulator, which is useful for studying the dynamical behaviour within the Bose Hubbard model. Note that the high numerical aperture is necessary for generating lattices suitable for Bose Hubbard type experiments since it is crucial to have lattices with small lattice spacing in order to get a significant tunneling parameter (recall from section 5.3, tunneling decreases exponentially with the lattice spacing). The high numerical aperture allows us to image the pattern onto the atoms with a significant demagnification.

We use two custom manufactured static phase patterns, as shown in Figure 6.1 that is deposited onto a glass substrate via photolithography. A beam passing through the line pattern would generate the corresponding diffraction orders. The diffraction orders from the two orthogonal line patterns are then combined on a polarization beam splitter

---

[1]Interfering beams necessarily generate periodic or semi periodic patterns
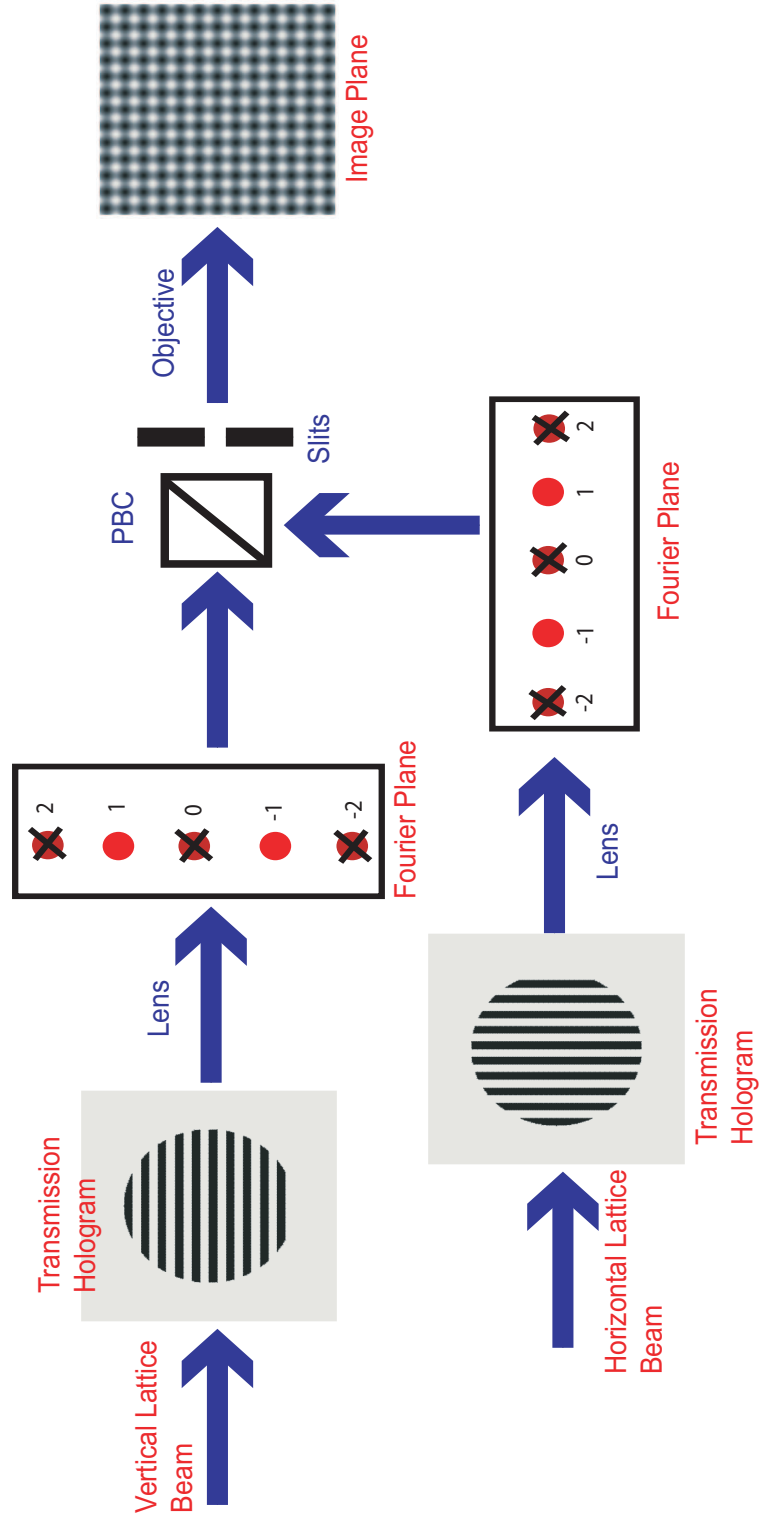
Figure 6.1: Schematics of setup to generate two dimensional optical lattice. Two oppositely polarized beams pass through orthogonally oriented transmission holograms. The holograms each contains lines with alternating phase shift of 0 and π with periodicity of 40 μm. After passing through the hologram, each beam splits into several diffraction order in the Fourier plane, the ± 1 orders are isolated and combined on a polarizing beam splitter cube. The four beams continue traveling down the imaging path and are combined by the microscope objective to interfere at the plane of the atoms to form a simple cubic lattice pattern.

cube. We then isolate the +1 and -1 orders which are combined to interfere at the location of the atoms using two stages of 4f imaging system with the microscope as the very last lens. Our choices of lenses, gives us a demagnification of 0.031, resulting in a lattice spacing of 620nm. Four slits are positioned just before the last Fourier plane outside of the objective. Their purposes are to remove high frequency components in the beams spatial structure, leaving behind a cleaner slowly varying Gaussian beam profile. The high frequency noise often arise from imperfection or dust particles in the beam path. Note the slits can only remove imperfections that occurs before it, so it is not able to correct for corrugations in the profile due to dusts in the objective itself.

The light source for the two dimensional lattice derive from a femtosecond laser centered at 757nm with full width half maximum of 5nm. The laser output was stretched out in time as described in Appendix B to avoid excessive spectral broadening when passing through a single mode fiber. The use of broadband light source allows us to mitigate the effects of stray reflection from glass surfaces situated close to the atom's location in the experiment, which is important for creating known and smooth lattice potentials.

To roughly focus the lattice beams to the right location, we first focus the Ixon camera shown in Figure 6.2 to the plane of the atoms using the fluorescence signal of the atoms in the two dimensional trap. We then overlay the reflection of the lattice beam from the flat surface of the hemisphere to be at the same location on the camera as the location of the atoms. This gives us only a rough positioning of the lattice beams due to the non-negligible focal shift from 780 nm (atom's fluorescence wavelength) to 757 nm (optical lattice wavelength). However we can get close enough for the lattice beam coverage to encompass the entire atomic cloud. A more precise alignment was then performed using the atoms by looking at the direction of atom outflow when the lattice deconfinement overcomes the red dipole confinement. The optimal position minimizes the gradient experienced by the
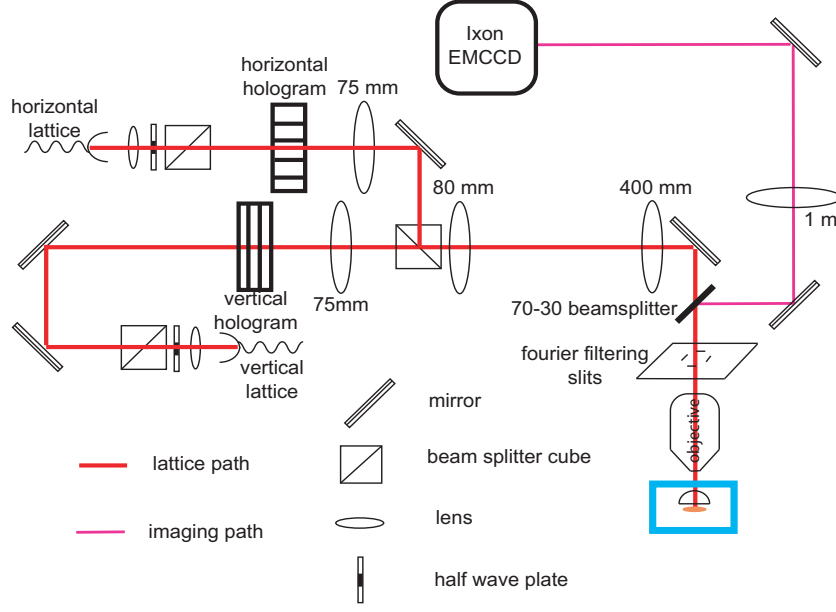
Figure 6.2: Schematics of setup for creating two dimensional optical lattice and fluorescence imaging of the atoms.

atoms, or the directional flow of the atom leakage.

After positioning the atoms in the correct location, we calibrate the lattice depth by pulsing the lattice beams onto the atoms for a variable period of time t_{pulse} [22, 31]. For t_{pulse} much shorter than the inverse recoil frequency of the atoms, the atoms will not have enough time to redistribute themselves in response to the light field, the BEC wavefunction thus evolve according to the stark shift provided by the lattice beams

$$|\psi_{BEC}\rangle \quad \rightarrow \quad |\psi_{BEC}\rangle e^{-\frac{i}{\hbar}\int_0^{t_{pulse}} \frac{V_L}{2}(1-\cos(2kx))\,dx} \tag{6.1}$$

$$= \quad |\psi_{BEC}\rangle\, e^{-\frac{iV_L t_{pulse}}{2\hbar}} \sum_{n=-\infty}^{\infty} i^n J_n\left(\frac{V_L t_{pulse}}{2\hbar}\right)\, e^{in2kx} \tag{6.2}$$

we see that the BEC is split into plane waves separated by twice the lattice wavevector $2k$ and the population in each diffraction order n is given by $|J_n(\frac{V_L t_{pulse}}{2\hbar})|^2$. We calibrate the lattice depth V_L at a fixed lattice power by finding the corresponding pulse time that minimizes the zeroth order.

6.2 Adiabatic Loading Into Optical Lattice

We want to load the atoms into the optical lattice in such a way that the wavefunction of the condensate remains in the many body ground state at all times. In order to accomplish this, the time over which the lattice ramps up must be adiabatic with respect to two time scales.

The first adiabatic criteria, requires that the ramp be slow enough such that the atoms remain in the lowest energy n=0 band. From the general adiabatic condition, we therefore require [22, 23]

$$|\langle n,q| \frac{d}{dt} |0,q\rangle| \ll \frac{|E_{n,q} - E_{0,q}|}{\hbar} \tag{6.3}$$

We need only consider the contribution from the $n = 1$ band, since it is the one closest in energy to the $n = 0$ band which we wish to populate. Furthermore, only $q = 0$ need be considered as we work with condensates that are loaded into a stationary lattice from rest, so populating mostly the $q = 0$ state with a spread $\delta q \ll k$ in quasi-momentum given by the inverse of the condensate size prior to loading which is much less than the size of the Brillouin zone. For this special case, equation (6.3) simplifies to

$$|\langle 1,0| \frac{d}{dt} |0,0\rangle| = \frac{\dot{V}_L}{2} \frac{\langle 1,0| \cos(2kx)|0,0\rangle}{E_{1,0} - E_{0,0}} \ll \frac{|E_{1,0} - E_{0,0}|}{\hbar} \tag{6.4}$$

Fortunately $|E_{1,0} - E_{0,0}|$ remains nonzero even at low lattice depth and is bounded below by $4E_R$ while $\langle 1,0| \cos(2kx)|0,0\rangle$ is bounded above by $1/\sqrt{2}$. We can therefore simplify (6.4) to

$$\frac{\dot{V}_L}{E_R} \ll \frac{32\sqrt{2}E_R}{\hbar} \tag{6.5}$$

Equation (6.5) implies that the characteristic time scale for lattice ramp to be adiabatic with respect to band structure is on order of $1/E_R$ which for our lattice structure, requires the ramp time to be longer than 675 μs.

The second adiabatic criteria requires the condensate to stay in the many body Hamiltonian's ground state which demands a much longer time scale [24]. For atoms in optical lattice, there are three relevant time scales to consider : the energy associated with the "external confinement" of frequency ω_{tot} which in our case arise from a combination of an auxiliary red detuned (see section 4.5) dipole beam plus an overall deconfinement from the blue detuned lattice beams, the onsite repulsive energy U and the tunneling time in the lattice J. The effects of changing U and ω_{tot} during the lattice ramp up is to modify the equilibrium Thomas Fermi size of the condensate which necessitate atom redistribution during the ramp in order to remain in the many body ground state. In order to counteract this effect, we compute numerically the increase in U and lattice deconfinement as a result of the increase in lattice depth using the expression (5.9) and (5.4) from the tight binding approximation. We then increase the red dipole frequency during the ramp in such a way that U/ω_{tot}^2 remains constant throughout the ramp. From section 5.4, this then ensures that the Thomas Fermi radii for the condensate in the superfluid regime remains constant during the lattice ramp up. We test this by imaging the condensate afterwards with the lattice ramped slowly in this way to various superfluid lattice depths.

The longest time scale requires adiabaticity with respect to the tunneling time in the lattice. The general adiabatic theorem suggests the criteria [24]

$$\max\left[\frac{\hbar|\dot{J}|}{J^2}\right] \ll 1 \tag{6.6}$$

We can roughly estimate the time scale required by using the analytical estimate of [25]

$$\frac{J}{E_R} \approx \sqrt{\frac{8}{\pi}}\left(\frac{V_L}{E_R}\right)^{3/4} e^{-2\sqrt{\frac{V_L}{E_R}}} \tag{6.7}$$

and our lattice ramp form

$$V_L(t) = V_L^F 10^{\alpha(t/\tau_{ramp}-1)} \qquad \alpha = 6.26$$

with V_L^F the final lattice depth, the condition (6.6) then requires that

$$\tau_{ramp} \gg \alpha \log(10) \sqrt{\frac{V_L^F}{E_R}} \frac{\hbar}{J} \tag{6.8}$$

To get an estimate of the time required for the ramp, we use the tunneling and lattice depth at the superfluid to mott insulator transition point since redistribution of atoms to the new equilibrium size will be strongly suppressed in the mott insulator regime. With a lattice depth of $V_L^F = 12 E_R$ the time required is $\tau_{ramp} \gg 536$ ms.

The adiabatic criterium place a lower bound on the time for lattice ramp, an upper bound also exists since too slow ramp leads to heating of the atoms during the loading process. It is unclear whether the source of the heating is due to spontaneous emission from the atoms (there are some evidence that this is the cause for a red detuned lattice, see [24]) since in a blue detuned lattice, the atoms experience little of the light's intensity. There may also be technical source to the heating due to beam position fluctuation or intensity fluctuation.

6.3   Superfluid to Mott Insulator Transition

To recap, the experimental sequence consists of the following steps, illustrated in Figure 6.3

1. MOT loading, molasses cooling and transport of atoms from the MOT chamber to the science chamber. After end of transport, 24s of RF evaporation takes place ending in the production of a Bose Einstein Condensate of atoms in a cigar shaped magnetic trap.

2. The center of the magnetic trap is shifted upwards towards the hemisphere while the intensity of the 10 μm spacing lattice is increased. At the end of this step most of the atoms are loaded into the 10 μm lattice.
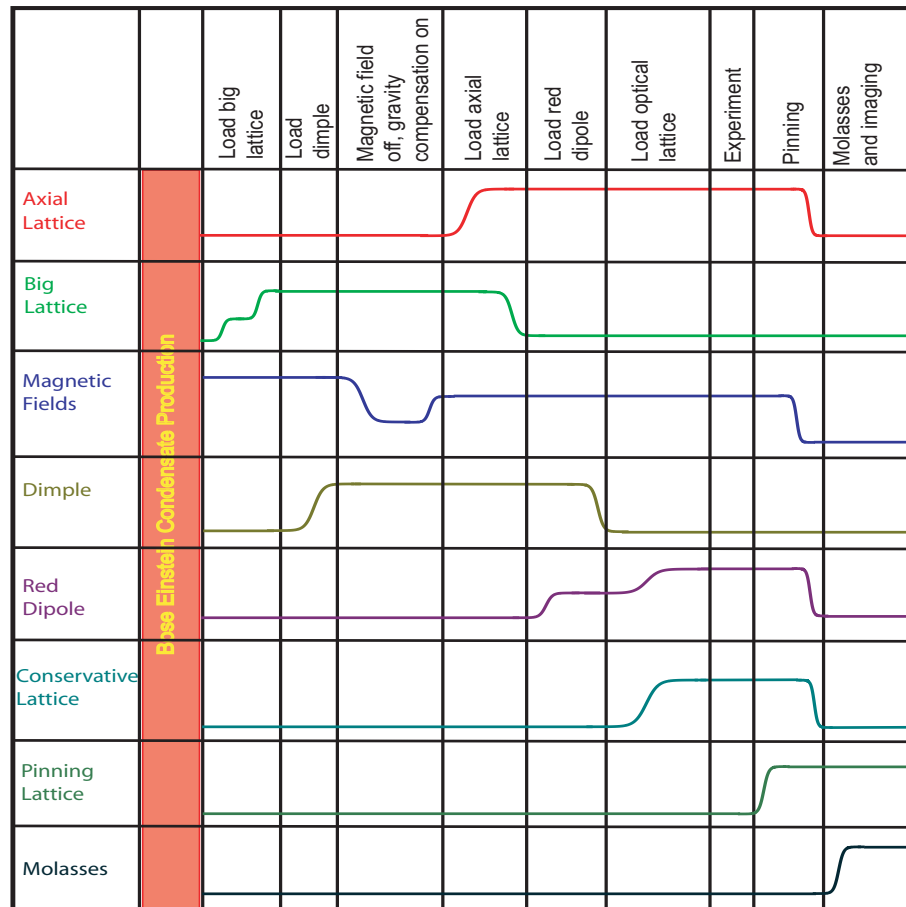
Figure 6.3: Sequence of events for optical lattice experiment.

3. The small volume red detuned dimple beam turns on after which all magnetic fields are switched off completely for 100 ms to allow the atoms not held in the dimple to escape the region. After the wait time, magnetic fields which null the gradient due to gravity are turned on. [2]

4. The atoms are transferred from the 10 μm lattice to the 1.5 μm vertical lattice (axial lattice).

5. The atoms are release from the small dimple into the large volume red dipole trap. At this point we have a two dimensional condensate of about 2000 atoms with vertical trap frequency of 7.1 kHz provided by the axial lattice and transverse confinement of 20 Hz provided by the red dipole.

6. The two dimensional optical lattice ramps on, at the same time the red dipole power is also increased to keep the Thomas Fermi radius of the trap constant during the ramp. Then experiment is performed.

7. When imaging is ready to be performed, we turn on the near resonant pinning lattice, molasses beams, and magnetic fields nulling current. After waiting 50 ms for the atoms to equilibrate in this configuration, the camera is exposed for 1s to collect fluorescence from the atoms.

Our first experiment is to look for evidence of superfluid to mott insulator transition. One of the most commonly used signatures is via loss of coherence as one crosses the transition point [26, 28, 27]. After a long time of flight (neglecting the effects of interaction during expansion), the atomic density distribution $n_{TOF}(\mathbf{r})$ is related to the in-situ

---

[2]The plane of the atoms is defined by the hemisphere whose center axis is tilted by about 0.6 degrees from the direction of gravity

wavefunction via

$$
\begin{aligned}
n_{TOF}(\mathbf{r}) \quad &\propto \quad \left| \int \psi(\mathbf{r}') \, e^{i\frac{m\mathbf{r}}{\hbar t}\cdot\mathbf{r}'} \, d^2\mathbf{r}' \right|^2 \\
&= \quad \sum_k \sum_j \langle \hat{b}_k^\dagger \hat{b}_j \rangle \, e^{i\frac{m\mathbf{r}}{\hbar t}\cdot(\mathbf{r}_j - \mathbf{r}_k)} \left| \tilde{w}\left(\frac{m\mathbf{r}}{\hbar t}\right) \right|^2
\end{aligned}
\tag{6.9}
$$

The qualitative behaviours in the two regimes is encapsulated in the sum

$$
S = \sum_k \sum_j \langle \hat{b}_k^\dagger \hat{b}_j \rangle \, e^{i\frac{m\mathbf{r}}{\hbar t}\cdot(\mathbf{r}_j - \mathbf{r}_k)}
\tag{6.10}
$$

in the case of the superfluid, the two site coherence is simply a constant $\langle \hat{b}_k^\dagger \hat{b}_j \rangle = \alpha$ so that S exhibits peaks at positions corresponding to the reciprocal lattice vector $\frac{m\mathbf{r}}{\hbar t} \cdot a_L = 2\pi$ owing to the periodicity of the lattice structure. In the case of the Mott insulator, the correlation tends to a delta function $\langle \hat{b}_k^\dagger \hat{b}_j \rangle = n_k \delta_{kj}$ so that S reduces to a constant and $n_{TOF}(\mathbf{r})$ is structureless except for the broad envelope corresponding to the Fourier transform of the Wannier function.

In figure 6.4, we show the time of flight images of atoms released from the optical lattice at various lattice depths. The secondary peaks corresponding to the reciprocal lattice vectors could clearly be seen at lattice depths below $12 - 14E_R$ which closely match the theoretical transition point of $12E_R$. This demonstrates that the different lattice sites maintain phase coherence with each other. Beyond $14E_R$, the system enters a Mott insulator state and only an unstructured broad envelope corresponding to the atoms' wavefunction (Wannier function) is seen, demonstrating the loss of global phase coherence as we cross the transition.

6.4   Outlook - Future Experiments

Further demonstration of the superfluid to mott insulator transition could be attained by looking at the change in atom number statistics as the transition point is crossed.
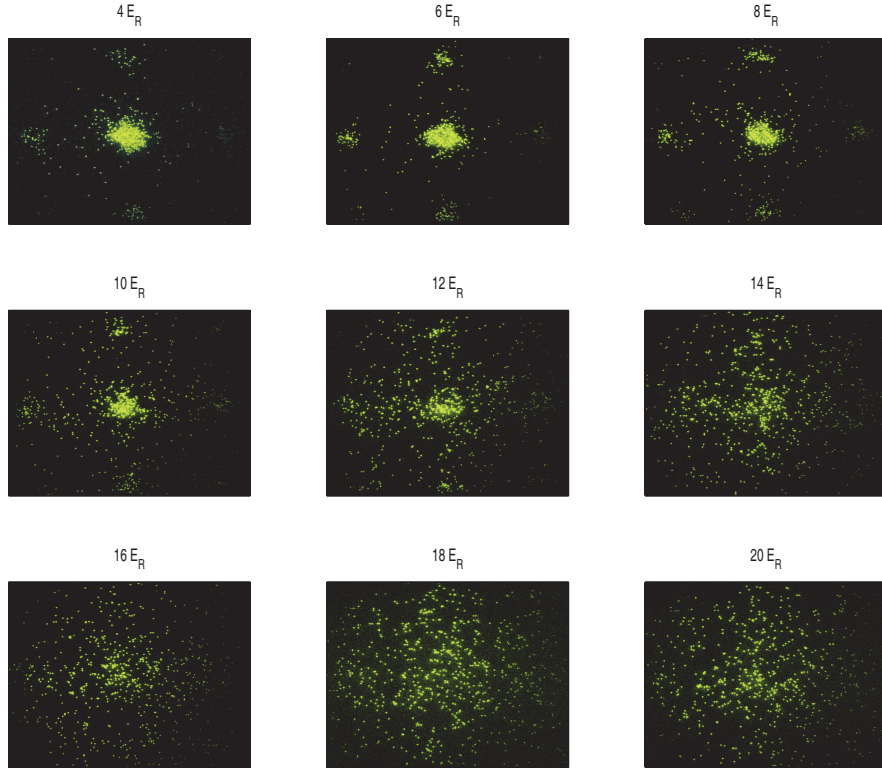
Figure 6.4: Fluorescence images of atoms released from the lattice. The lattice is ramped up exponentially over 400ms to the final depth as labeled above each picture, and held in lattice for 20 ms before releasing the horizontal confinement allowing the atoms to expand in the plane for 9ms prior to imaging. The right peak in the superfluid images has lower signal owing to the weaker molasses beam intensity in that region. The superfluid to mott insulator transition point occurs at $12E_R$ lattice depth.

As mentioned in section 5.4, the superfluid state is characterised by a coherent state number statistics at each site, hence we expect a poissonian distribution for the site occupation

$$Pr(n_i = s) = e^{-\overline{n}_i} \; \frac{(\overline{n}_i)^s}{s!}$$

where $\overline{n}_i$ is the mean occupation of site i. As our detection method gives only parity of atom number, we expect to measure a mean atom number of $e^{-\overline{n}_i} \; sinh(\overline{n}_i) < 0.5$ per lattice site in the superfluid state. In the mott insulator state, the suppression of tunneling lead to a Fock state of atom number per lattice site, so that our measured mean atom number is

$$if \;\; \overline{n}_i \in odd \;\; \rightarrow \;\; 1$$

$$if \;\; \overline{n}_i \in even \;\; \rightarrow \;\; 0$$

Hence a measured occupation per site greater than 0.5 would indicate a non poissonian atom number distribution, implying the existence of a Mott insulator state. Figure 6.5 shows the average atom number per site over 100 images taken deep in the Mott insulator regime. Notice the annulus like region of high occupation interspersed by rings of low occupation. The spatial distribution resembles structures as one would expect from Mott insulator shells. We believe the non circularly symmetric structure arise primarily due to corrugations in the lattice beam profile after passing through the dusty objective.
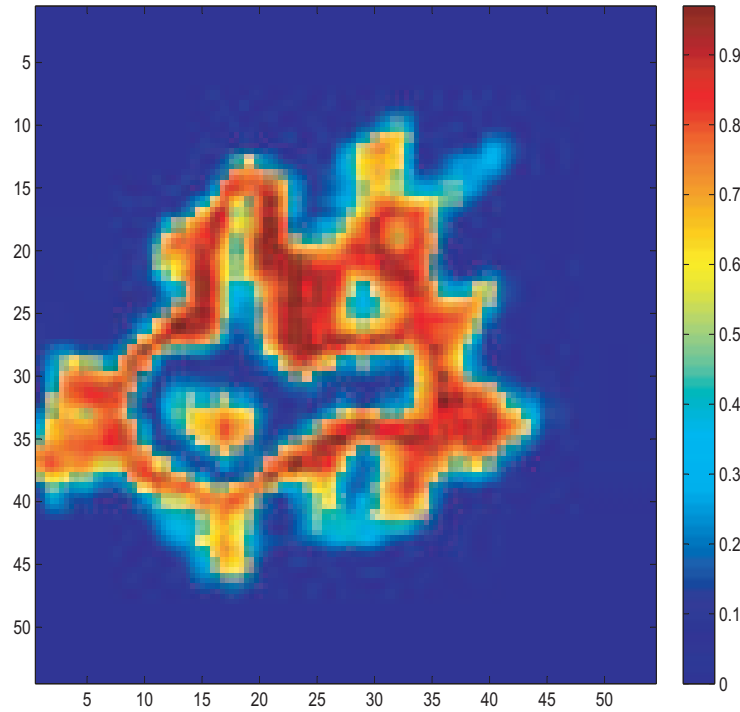
Figure 6.5: Average site occupation over 100 experiment runs. The red regions with high occupation is indicative of non-poissonian number statistics pointing to the existence of Mott insulator state.

Bibliography

[1] P. W. Pinkse, A. Mosk, M. Weidmuller, M. W. Reynolds, T. W. Hijmans, and J. T. Walraven *Phys. Rev. Lett.*, **78**:990, 1997.

[2] M. Hammes, D. Rychtarik, H. -C. Nagerl, and R. Grimm *Phys. Rev. A*, **66**:051401, 2002.

[3] D. M. Stamper-Kurn, H. -J. Miesner, A. P. Chikkatur, S. Inouye, J. Stenger, and W. Ketterle *Phys. Rev. Lett.*, **81**:2194, 1998.

[4] T. Kinoshita, T. Wenger and D. S. Weiss *Phys. Rev. A*, **71**:011602(R) 2005.

[5] H. F. Hess *Phys. Rev. B*, **34**:3476, 1986.

[6] K. B. Davies, M. O. Mewes, and W. Ketterle *Appl. Phys. B*, **60**:155, 1995.

[7] Z. Ma, C. J. Foot, and S. L. Cornish *J. Phys. B*, **37**:3187, 2004.

[8] T. Weber, J. Herbig, M. Mark, H-C Nagerl, and R. Grimm *Science*, **299**:232, 2003.

[9] Bose *Zeitschrift Fur Physik*, **26**:178, 1924

[10] I. Walmsely, L. Waxer, and C. Dorrer *Review of Scientific Instruments*, **72**:1, 2001

[11] Neil. W. Ashcroft and N. D. Mermin Solid State Physics, 1976

[12] D. Jatsch, C. Bruder, J. I. Cirac, C. W. Gardiner, and P. Zoller *Phys. Rev. Lett.*, **81**:3108, 1998

[13] M. P. A. Fisher, P. Weichman, G. Grinstein, and D. S. Fisher *Phys. Rev. B*, **40**:546, 1989

[14] Subir Sachdev Quantum Phase Transition, 2001

[15] Nathan Gemelke, Xibo Zhang, Chen-Lung Hung and Cheng Chin *Nature*, **460**:995, 2009

[16] I. B. Spielman, , W. D. Phillips and J. V. Porto *Phys. Rev. Lett.*,**100**:120402, 2008

[17] I. B. Spielman, , W. D. Phillips and J. V. Porto *Phys. Rev. Lett.*,**98**:080404, 2007

[18] S. Foelling, A. Widera, T. Muller, F. Gerbier and I. Bloch *Phys. Rev. Lett.*,**97**:060403, 2006

[19] G. Campbell, J. Mun, M. Boyd, P. Medley, A. Leanhardt, L. Marcassa, D. E. Pritchard, and W. Ketterle *Science*, **313**:649, 2006

[20] S. M. Mansfield and G. S. Kino *Appl. Phys. Lett.*, **57**:2615, 1990

[21] N. Teichmann, Dennis Hinrichs, M. Holthaus and A. Eckardt *Phys. Rev. B*,**79**:100503, (2009)

[22] J. Hecker Denschlag, J. E. Simsarian, H. Haffner, C. McKenzie, A. Browaeys, D. Cho, K. Helmerson, S. L. Rolston, and W. D. Phillips *J. Phys. B: At. Mol. Opt. Phy.*,**35**:3095, (2002)

[23] M. Ben Dahan, E. Peik, J. Reichel, Y. Castin and C. Salomon *Phys. Rev. Lett.*,**76**:4508, (1996)

[24] T. Gericke, F. Gerbier, A. Widera, S. Folling, O. Mandel, and I. Bloch *arXiv:cond-mat*:0603590, (2006)

[25] W. Zwerger *J. Opt. B*, **5**:S9, (2003)

[26] M. Greiner, O. Mandel, T. Esslinger, T. W. Hnsch, I. Bloch *Nature*, **415**:39, (2002)

[27] F. Gerbier, A. Widera, S. Flling, O. Mandel, T. Gericke, and I. Bloch *Phy. Rev. Lett.*, **95**:050404, (2005)

[28] K. Xu, Y. Liu, J. R. Abo-Shaeer, T. Mukaiyama, J. K. Chin, D. E. Miller, and W. Ketterle *Phys. Rev. A*, **72**:043604, (2005)

[29] F. Gerbier *Phys. Rev. Lett.*, **99**:120405, (2007)

[30] D. van Oosten, P. van der Straten, and H. T. C. Stoof *Phys. Rev. A*, **63**:053601, (2001)

[31] G. Campbell *Ph. D. Thesis*, (2008)

[32] P. C. Hohenberg *Phys. Rev.*, **158**:383, (1967)

[33] N. D. Mermin and H. Wagner *Phys. Rev. Lett.*, **17**:1133, (1966)

[34] C. J. Pethick and H. Smith *Bose Einstein Condensation in Diulte Gases*, Cambridge University Press (2008)

[35] Y. Shin, C. H. Schunck, A. Schirotzek, and W. Ketterle *Phys. Rev. Lett.*, **99**:090403, (2007)

[36] M. H. Anderson, J. R. Ensher, M. R. Matthews, C. E. Wieman and E. A. Cornell *Science*, **269**:198, (1995)

[37] C. C. Bradley, C. A. Sackett, J. J. Follet and R. G. Hulet *Phys. Rev. Lett.*, **75**:1687, (1995)

[38] K. B. Davis, M. O. Mewes, M. R. Andrews, N. J. van Drute, D. S. Durfee, D. M. Kurn and W. Ketterle *Phys. Rev. Lett.*, **75**:3969 (1995)

[39] B. DeMarco and D. D. Jin *Science*, **285**:1703, (1999)

[40] F. Schreck, K. L. Khaykovich, G. Corwin, G. Ferrari, T. Bourdel, J. Cubizolles, and C. Salomon *Phys. Rev. Lett.*, **87**:080403, (2001)

[41] A. Truscott, K. Strecker, W. McAlexander, G. Patridge, and R. Hulet *Science*, **291**:2570, (2001)

[42] W. Hofstetter, J. I. Cirac, P. Zoller, E. Demler, and M. D. Lukin *Phys. Rev. Lett.*, **89**:220407, (2002)

[43] B. Paredes, and J. I. Cirac *Phys. Rev. Lett.*, **90**:150402, (2003)

[44] T. Kinoshita, T. Wenger, and D. Weiss *Science*, **305**:1125, (2004)

[45] M. Greiner, I. Bloch, O. Mandel, T. W. Hansch and T. Esslinger *Apply. Phys.*, **B73**:769, (2001)

[46] M. Kohl, H. Moritz, T. Stoferle, K. Gunter, and T. Esslinger *Phys. Rev. Lett.*, **94**:080403, (2004)

[47] F. S. Cataliotti, S. Burger, C. Fort, P. Maddaloni, F. Minardi, A. Trombettoni, A. Smerzi, and M. Inguscio *Science*, **293**:843, (2001)

[48] W. S. Bakr, J. I. Gillen, A. Peng, S. Folling, and M. Greiner *Nature*, **462**:74, (2009)

[49] R. P. Feynman *Opt. News*, **11**:11, (1985)

[50] R. P. Feynman *Found. Phys.*, **16**:507, (1986)

[51] G. Baym and C. J. Pethick *Phys. Rev. Lett.*, **76**:6, (1996)

[52] F. Dalfovo, S. Giorgini, L. P. Pitaevskii, and S. Stringari *Rev. Mod. Phys.*, **71**:463, (1999)

[53] R. Grimm, M. Weidmuller and Y. B. Ovchinikov *Adv. At. Mol. Opt. Phys.*, **42**: 95, (1999)

[54] J. Dalibard and C. Cohen-Tannoudji *J. Opt. Soc. Am. B*, **2**:1707, (1985)

[55] M. T. DePue, C. McCormick, S. L. Winoto, S. Oliver, and D. S. Weiss *Phys. Rev. Lett.*, **82**:2262, (1999)

[56] J. I. Gillen *Quantum gas microscope*, Ph.D. Thesis, Harvard University (2009)

[57] J. I. Gillen, W. S. Bakr, A. Peng, P. Unterwaditzer, S. Flling, and M. Greiner *Phys. Rev. A*, **80**:021602, (2009)

[58] A. Klinger, S. Degenkolb, N. Gemelke, K. Brickman Soderberg, C. Chin *arXiv:quant-ph*, 0909.2475 (2009)

[59] R. Newell, J. Sebby, and T. G. Walker *Opt. Lett.*, **28**:1266, (2003)

[60] S. Bergamini, B. Darquie, M. Jones, L. Jacubowiez, A. Browaeys, and P. Grangier *J. Opt. Soc. Am. B*, **21**:1889, (2004)

[61] S. L. Cornish, N. R. Claussen, J. L. Roberts, E. A. Cornell, and C. E. Wieman *Phys. Rev. Lett.*, **85**:1795, (2000)

[62] P. O. Fedichev, M. W. Reynold, and G. V. Shlyapnikov *Phys. Rev. Lett.*, **77**:2921, (1996)

[63] M. Greiner and S. Foelling *Nature*, **453**:736, (2008)

[64] I. Bloch *Nature Physics*, **1**:23, (2005)

[65] C. Waschke, H. Roskos, R. Schwedler, K. Leo, H. Kurz, and K. Khler *Phys. Rev. Lett.*, **70**:3319, (1993)

[66] F. Bloch *Z. Phys.*, **52**:555, (1929)

[67] C. Zener *Proc. R. Soc. London A*, **145**:523, (1934)

[68] P. Wurtz, T. Langen, T. Gericke, A. Koglbauer, and H. Ott *Phys. Rev. Lett.*, **103**:080404, (2009)

[69] T. Gericke, P. Wurtz, D. Reitz, T. Langen, and H. Ott *Nature Physics*, **4**:949, (2008)

[70] K. Nelson, X. Li, and D. Weiss *Nature Physics*, **3**:556, (2007)

[71] J. M. McGuirk, D. M. Harber, J. M. Obrecht, and E. A. Cornell *Phys. Rev. A*, **69**:062905, (2004)

Appendix A

Intensity Stabilisation

For all the dipole traps and lattice beams used in the experiment, it is important to actively stabilise the intensity, as residue fluctuations leads to time varying modulations and can lead to heating of atoms. For the red dimple and red dipole beams it is especially important as we use the light power to control the atom number and temperature in the 2D trap.

In order to lock the laser powers over the range of a few orders of magnitudes, we extract a small portion of the beam after the fiber output on the experiment table and direct it to a logarithmic photodiode. For this, we use a silicon photodiode (BPX65) connected to a logarithmic amplifier (Analog Devices AD8304) with modifications to give a slope of 500 mV per decade. That is the photodiode output voltage is $V_{LOG} = 0.5 \log_{10} P_{in}/P_0$ where $P_0 = 1.8 \times 10^{-7}$ mW. The use of a logarithmic photodiode allows us to lock the intensity over a range of five orders of magnitude in laser power. The output voltage of the photodiode is then fed into the input signal port of a specially designed PI loop, whose output actuates an exponential amplifier (Analog Devices ADL 5330) that controls the RF power driving an acousto-optic modulator (AOM). The first order of the AOM is used for
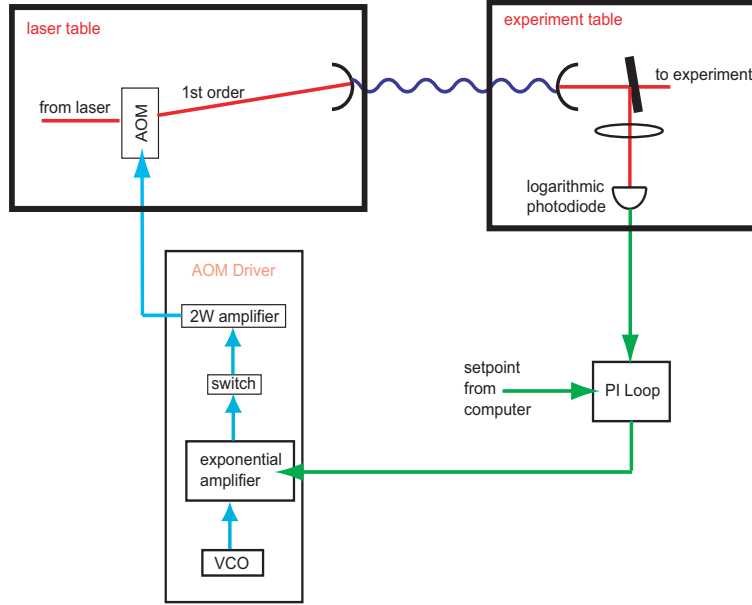
Figure A.1: Schematic of the laser intensity locking schematic. The laser power is controlled via RF power to an acousto optic modulator (AOM) on the laser table. A portion of the laser light at the experiment table is tapped off with a beam sampler and directed to a logarithmic photodiode whose output is directed to a homemade PI circuitry. The output of the lock circuitry is used to actuate an AOM driver incorporating an exponential amplifier in order to lock the laser intensity to computer specified values.

the experiment. The schematic of the setup is depicted in Figure A.1.

The main protagonist of the stabilisation setup is the specially designed PI circuitry whose schematic is illustrated in Figure A.2. The circuit consists of four major blocks where the output of each block is given as the input to the next block. In the order in which they are implemented, they are P, I, rectifier which prevents the output voltage from being negative and upper limit restriction that ensures the out voltage is less than the 7V limit of the exponential amplifier. The appropriate P,I values is determined by the system's response function which was measured separately.

We find that the servo loop is able to lock to control signals all the way up to 5 kHz in modulation. In locking to a square pulse of frequency 1 kHz, the servoed intensity
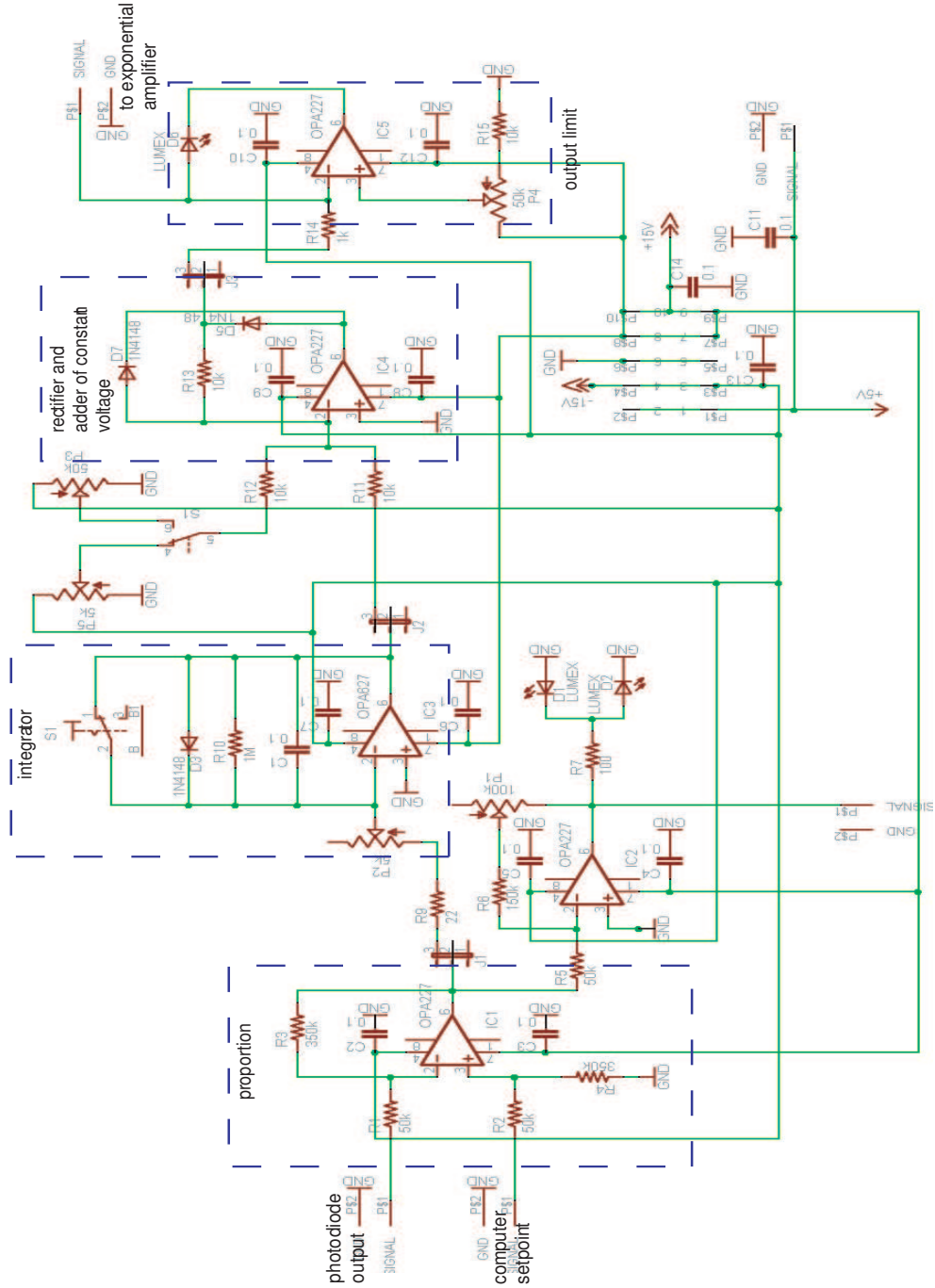
Figure A.2: Schematic of circuitry used to stabilise intensity of laser beam to computer specified set point.

has a rise time of 28 μs and fall time of 26 μs. A measurement of the residue noise on the servoed light using an independent photodiode shows the rms intensity noise is 0.04 % mostly above 10 kHz in frequency.

Appendix B

Pulsed Laser

Due to the large number of glass surfaces in our experiment close to the vicinity of the atoms, we are very susceptible to the intensity modulations due to interference with uncontrolled reflected beams. The way we have chose to overcome this problem is to use light of short coherence length of broadband light. The idea is that any reflection that leaves from the atoms and return, provided it has traveled a distance longer than the coherence length of the laser, will no longer bear sufficient pahse correlation relative to the light at the atoms to be able to interfere with it.

All the dipole traps in our experiment are made using broadband light. One of our sources of broadband light for the experiment is a titanium sapphire femto/pico second pulsed laser (Coherent Mira pumped by a Verdi). The ultra-fast laser technology is an active field of research, its uses includes but are not limited to biomedical imaging, micromachining, femtochemistry and frequency combs that are used to spectroscopy and clock. There are several different methods of generating trains of short pulses but all of them relies on the combination of two elements :

- A medium in the laser cavity that promotes the gain of pulsed output. Usually this

utilises the high peak energy feature of the pulses or a frequency synchronisation to the repetition rate.

- Dispersion compensation within the cavity. This is essential since the different frequency components in the pulse must maintain a constant and well defined phase relative to each other for a pulse to remain the same shape during propagation. For most materials, this can be very difficult as dispersive effects upon reflection, refraction, interference or diffraction would lead to pulse broadening.

Our laser operates via a Kerr lensing effect. The large peak energy of the pulses causes the titanium sapphire crystal to act like a lens and leads to focusing of the beam. A slit is placed near the focus position so that only a focussed beam can pass. In this way, the formation of pulses is encouraged. Dispersion compensation is achieved via a pair of prisms which when placed in the right orientation relative to each other gives rise to anomalous dispersion to compensate for the normal dispersion due to all other optical elements in the laser cavity and hence maintain the pulse shape. We operate our laser in the femtosecond mode where the transform limited output has a time width of about $\tau_p = 150\,fs$ and a repetition rate of 75.4 MHz (determined by the physical length of the laser cavity). As with most Ti-Sapph lasers, the output intensity profile is of the form $I(t) = I_0 sech^2(1.76t/\tau_p)$.

Because the peak energy of the pulse is so high (about 90 kW) when focussed down to a small area, the large intensity can give rise to nonlinear effects in materials. Such is the case when we attempted to transport the output light via a single mode fiber (mode diameter $5\,\mu m$), the self phase modulation (i.e. dependence of refractive index on intensity) lead to the generation of many frequencies. As a result, the spectrum at the output of the fiber becomes very broad as shown in Figure B.1. In order to circumvent this problem, we
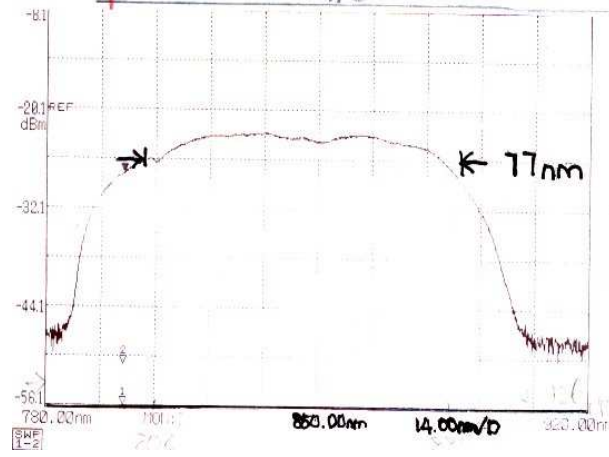
Figure B.1: Spectrum of pulsed laser after passing though 24m long single mode fiber. The spectral width is significantly increased due to the self phase modulation that occurs inside the fiber

reduce the peak power of the pulses by stretching it out in time. Although this happens naturally due to dispersion when light travel through materials, the physical size required to stretch the pulse sufficiently is simply too large to be practical, we therefore utilizes a technology commonly in pulse compression.

Consider the arrangements shown in Figure B.2 [10]. The output from the laser is incident upon a grating of line spacing d at angle γ to the grating normal. The first order diffraction travels at angle $\alpha(\lambda)$ to the normal and is dependent on the wavelength. Upon hitting the second grating we see that red light has traveled a longer path than blue light. An identical second grating G_2 collimates the beam so that all frequencies are traveling parallel to each other. The roof prism reflect the beam back in the same direction but displaced vertically below so that in total the pulse traverses the gratings 4 times and exits the stretched with almost the same profile as initially but now the frequencies have a greater phase difference with respect to each other.

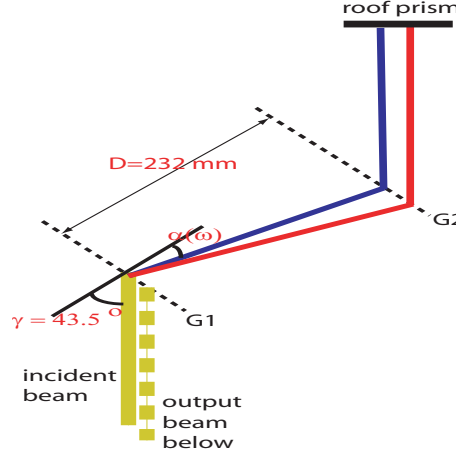The amount of phase shift due to distance traveled after the first grating is a

Figure B.2: Schematics of pulse stretcher setup. A gratings G1 with 1800 lines per mm separates the difference frequency components spatially by causing them to travel at different angles. A second identical grating G2 that is positioned parallel to G1 causes the frequencies to be laterally displaced with respect to each other but traveling parallel. A roof prism retro-reflect the beam while displacing it vertically down. The beam then pass through the two gratings one more time to exit the stretched below the incident beam.

function of frequency ω

$$\phi(\omega) = \frac{\omega}{c} \, \frac{L}{\cos \alpha(\omega)} \tag{B.1}$$

where L is the distance between the gratings measured along their normals. The group delay dispersion (characterising the change in group velocity per frequency of light) is given by the curvature of B.1 evaluated at the center frequency ω_c, $\phi''(\omega_c)$. The amount of pulse stretching after four passes is then

$$\tau = \frac{4\Delta\omega \, \phi''(\omega_c)}{\omega_c} = 4\frac{\lambda_c L \, \Delta\lambda}{cd^2 \cos^3 \alpha(\lambda_c)} \tag{B.2}$$

where $\Delta\lambda$ is the width of the incident pulse.

For our stretcher design, we calculate the final pulse width to be 94 ps. One can compare this to the pulse width of the same input after traveling 24m through synthetic fused silica, 15ps. We see that the stretched design using gratings is indeed far more efficient than using materials alone. As shown in Figure B.4, the output spectrum of the laser is
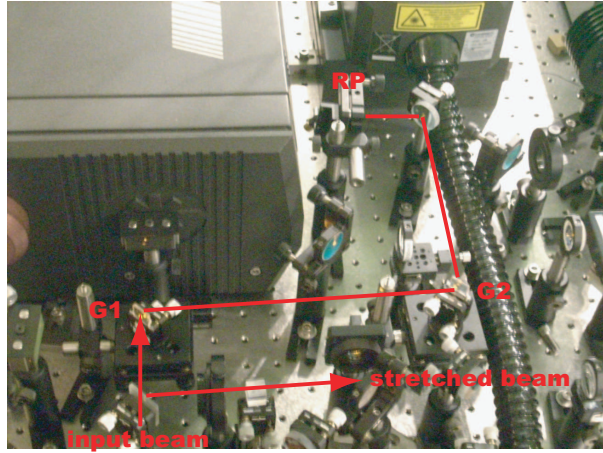
Figure B.3: Stretcher for pulsed laser. The red lines show the path of the laser beam in the stretcher. The return path of the beam is vertically displaced below the incident beam path. G1, G2 are the two gratings used (volume phase hologram gratings from Wasatch Photonics). RP is the roof prism for retro reflecting the beam
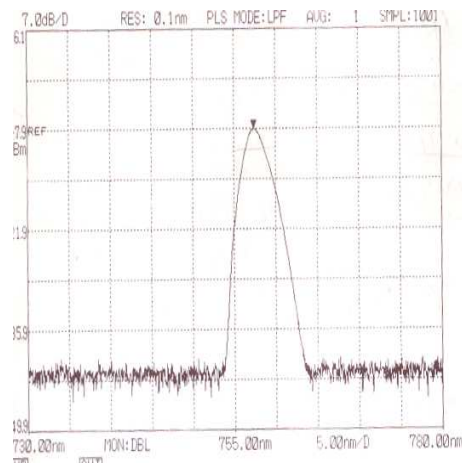
significantly improved.

Figure B.4: Spectrum of pulsed laser light at the experiment table